Shape optimization of the energy efficiency of building retrofitted facade

Sultan Alpar, Julien Berger, Walter Mazuroski, Rafik Belarbi

Sultan Alpar, Julien Berger, Walter Mazuroski, Rafik Belarbi. Shape optimization of the energy efficiency of building retrofitted facade. Solar Energy, 2024, 271, pp.112437. 10.1016/j.solener.2024.112437 . hal-04506263

HAL Id: hal-04506263
https://hal.science/hal-04506263v1

Submitted on 15 Mar 2024

Shape optimisation of the energy efficiency of building retrofitted facade

Sultan ALPAR [1, 2]*, Julien BERGER [1], Walter MAZUROSKI [3], Rafik BELARBI [1]

March 15, 2024

[1] Laboratoire des Sciences de l'Ingénieur pour l'Environnement (LaSIE), UMR 7356 CNRS, La Rochelle Université, CNRS, 17000, La Rochelle, France
[2] International Information Technology University (IITU), 34/1 Manas street, 050040, Almaty, Kazakhstan
[3] Pontifícia Universidade Católica do Paraná (PUCPR), Laboratório de Sistemas Térmicos (LST), Rua Imaculada Conceição, 1155, CEP. 80215-901, Curitiba, Paraná, Brasil
*corresponding author, e-mail address : sultan.alpar@univ-lr.fr

Abstract

The current state of research indicates a necessity of further examination in both numerical and experimental studies related to optimizing shapes of building enclosures for the enhancement of their energy efficiency. The demand for research primarily arises due to the numerical complexities associated with optimizing shapes for this specific purpose. Consequently, the primary objective of this article is to address and bridge these gaps in the field. To achieve this, a two-dimensional steady-state heat diffusion model is assumed to represent the physical processes occurring within building facades of varying shapes. A third type boundary condition is applied to the exterior boundary, encompassing convective and incident short-wave solar radiation effects. The calculation of short-wave radiation accounts for factors such as sunlight exposure and shading, influenced by the surrounding urban environment. The internal boundary interfaces with the indoor ambient air, and thus, a Robin boundary condition is adopted. To tackle the computational demands while ensuring accuracy, the boundary element method (BEM) is employed by discretizing the domain boundary into discrete elements. Then, two heat transfer design objectives are define according to the period of investigations: ones related to enhancing heat transfer and ones focused on thermal insulation problem. Last, a real-world case study is conducted, considering a house wall under varying climate conditions throughout the year. Optimal shapes for the external wall boundary are determined with the constraint that the optimized facade utilizes the same amount of material as the reference flat one. The results demonstrate a substantial increase in energy efficiency compared to the reference flat wall case.

Key words: steady-state heat transfer, boundary element method, shape optimization, short wave radiation.

1 Introduction

Buildings account for a 30% portion of global energy consumption and 26% greenhouse gas emissions according to statistic data provided by International Energy Agency (IEA), Paris, France in 2022 [1]. For the past 50 years, several models have been developed to represent the physical phenomena occurring building facade with the objective of designing high energy efficient enclosures [2–4]. A recent review has been proposed in [5]. Despite all the simulation programs developed, the building enclosures are often designed following two principles: *(i)* the enclosures are plane barriers created against the climatic varying outside conditions. It omits the fact that incident radiation and convective heat flux are not spread uniformly on the enclosure. The variation of the short wave radiation with the urban environment is generally disregarded for the facade design [6, 7]. Ana Paula de Almeida Rocha *et al.* and Mohammad Mirsadeghi *et al.* made some attempts for accurate shading assessment or convective heat transfer coefficient, as reported in [8] and [9], respectively. However, as Nicolas Lauzet *et al.* mentioned in [10], the actual building simulation tools cannot handle spatially variable boundary conditions. *(ii)* As a consequence, the enclosures are conceived using 1D model by association of multiple plane layers. Considering those two drawbacks, can the energy efficiency be improved by shape optimization of the building facade? Thus the main goal of this article is to investigate the possibility to optimize building shape.

Regarding state of the art on building facade shape improvement, there are many investigations and research findings. For instance in the work [11] Mohammad Jafari and Alice Alipour focus on shape optimization of high-rise buildings to minimize wind-induced loads. It employs computational tools and simulations to optimize building shapes for reduced wind effects. A multi-objective optimization approach is presented in [12] for sustainable high-rise building shapes, considering factors like energy efficiency, day lighting, and material use. One of the first challenges in shape optimization relies in the parametrization of the shape. Such parametrization can be broadly categorized into two types: continuous and discrete [13]. Continuous parameterization involves representing shapes using mathematical equations or functions. Continuous approach offers smooth transitions between shapes, precise representations, and easy application of mathematical operations, but it requires significant computational resources. For instance in the work of Yunfeng Luo *et al.* [14] level-set sinus function is used for the adjoint-based optimization of thermohygrometric performance for pin-fin array geometry in 3D transient fluid. Authors maximize the ratio of heat transfer and pumping factor. Jeong-Tak Jin and Jae-Weon Jeong showed another example of continuous parameterized shapes in [15], where geometric modeling of a free-form building surface was performed using continuous design models in Rhinoceros program. Then, the thermal load of a building is estimated using TRNSYS software to optimize the heat gain variation. The heat balance method is used by TRNSYS as a base for all calculations. In contrast, second approach - discrete parameterization employs a finite set of parameters, which describe various characteristics of the shape, such as size, curvature and other geometric properties. Thus, it makes discrete parameterization suitable for representing complex shapes from real world or when mathematical equations are not applicable. However, it explores only a reduced part of the parameter domain and may miss some optimal shape in the process. This method is broadly used for solving multiple engineering shape optimization problems than continuous approach. In [16] corner recession discrete plan shapes are used to reduce wind loads on buildings using Computational Fluid Dynamics tools. Similar investigations are made by Shuai Zhang *et al.* in [17], where discrete insulation corner wall envelopes are employed to minimize energy consumption in buildings by examining the transient fluid flow in 2D regime. There are plenty other works with different selections of discrete parameterized shapes: discrete response surfaces for aeroelastic performance optimization [18], two-dimensional cylinders multi-objective optimization approach for sustainable high-rise building shapes with different corner recessions for aerodynamic optimization [19] or even series of sample building shapes with twisting modifications [16].

A second challenge in shape optimization is the modelling of physical phenomena in the building enclosures. To our best knowledge, most of the work neglect or simplify the heat transfer through solid walls in the optimization process [20]. On the one hand the review articles about shape optimization techniques [21, 22] illustrate that the majority of studies predominantly focus on fluid flow dynamics around building enclosures. On the other hand [23–26] demonstrate that there are plenty of examples of studies on facade building shape optimization which are focused on energy efficiency. But common drawback is when authors consider isothermal condition on the solid surfaces (see for instance [16–19, 27]). Thus, it misses the crucial aspect of the energy balance played by solid facade between the inside and outside environment. When considering the heat balance, the studies generally simplify the equation considering a lumped approach based on transfer function method [28, 29]. In such approach, the assumption of steady-state conditions is made, which may lack of accuracy for precise assessment of the energy efficiency. Moreover, another noticeable gap in the existing work relates to the limited attention given to the impact of solar radiation on the shape and design of buildings. While Mayssa Dabaghi *et al.*, Longwei Zhanghave *et al.* and Rabee M. Reffat *et al.* made significant strides in optimizing building shape structures [30–32], a comprehensive understanding of how solar radiation influences surface morphology remains largely unexplored. This represents a critical area where further investigation and research are warranted to unlock innovative design possibilities that can harness solar energy more efficiently and enhance the sustainability of architectural solutions [33, 34].

This analysis of the state of the art reveals two challenges to be tackled: building shape optimization needs to consider the *(i)* influence of the solid facade shape design on the energy balance between inside and outside environment, *(ii)* the influence of the spatial variation of the incident solar short wave radiation on the building facade. In order to bridge the existing gaps in the field of building shape optimization, this research considers investigation of heat transfer mechanisms through building walls. The approach chosen in this article takes into consideration the impact of incident short wave radiation, accounting for variations in solar exposure on the wall surface due to urban environment such as neighboring buildings [35]. Furthermore, a continuous description of the building wall shape is incorporated. It enables consistent interpolation, compatibility with optimization algorithms, and accurate modeling in simulations. To facilitate the computational efficiency of our analysis while ensuring robust and dependable outcomes, the boundary element method (BEM) has been employed. This method serves as a powerful tool for solving the steady-state heat equation, reducing computational overhead without compromising the accuracy of our results [36].

The article organized as follows. Section 2 presents the governing equations with appropriate boundary conditions. It follows with description of solar radiation modeling using analytical projection method. Then the dimensionless formulation of the governing equations is presented with application of the boundary element method. Section 3 describes the design optimization problem. Then, Section 4 aims at verifying the short wave radiation modeling using the pixel counting technique as a reference solution. It follows with BEM verification with analytical solutions. Finally, in Section 5 a real case study for shape facade improvement during winter and summer periods.

2 Methodology

2.1 Physical domain

The physical domain under investigations is illustrated in Figure 1. The domain is denoted by Ω with space coordinates $\boldsymbol{x} = (x, y)$. The height of the facade is $H\ [\mathrm{m}]$. The boundary of the domain is $\Gamma = \cup_{i=1}^{4} \Gamma_i$. The bottom, right and top boundaries are denoted as Γ_2, Γ_3 and Γ_4, respectively. The left boundary is Γ_1 and is defined by:

$$\Gamma_1(\boldsymbol{p}) = \{ \boldsymbol{x} \in \mathbb{R}^2 \,|\, x = \gamma(\boldsymbol{p}, y),\, y \in [0, H],\, \boldsymbol{p} \in \Omega_p \}, \tag{1}$$

where $\gamma(\boldsymbol{p}, y)$ is a parametrized mapping function, which shapes the form of the boundary Γ_1 depending on the N_p parameters:

$$\boldsymbol{p} = (p_1, \dots, p_{N_p}) \in \Omega_p .$$

Note that in the case $\gamma(\boldsymbol{p}, y) = 0$, we have a plane boundary Γ_1 and the facade is a classical rectangular one. In such case, the length of the wall is denoted $L\ [\mathrm{m}]$.

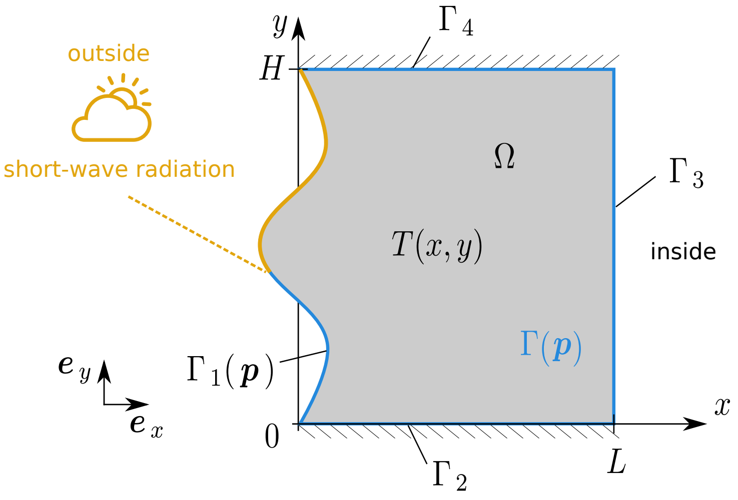

Figure 1. *Illustration of the physical domain.*

2.2 Governing equations

The two-dimensional steady-state heat diffusion transfer is assumed to represent the physical phenomena in the building facade:

$$\boldsymbol{\Delta} T \,=\, 0\,, \qquad \forall \boldsymbol{x} \,\in\, \Omega\,,$$

where $T \; \bigl[\,\mathrm{K}\,\bigr]$ is the temperature inside the facade. The left boundary is in contact with the outside environment of the building. Combining NEWTON's law of heat transfer with FOURIER's first law of conduction and adding the incident short-wave solar radiation leads us to a third-type boundary condition also known as ROBIN boundary condition:

$$k\,\boldsymbol{\nabla} T \cdot \vec{n} \,=\, -\,h_L^{\infty}\,(\,y\,)\,(\,T \,-\, T_L^{\infty}\,) \,+\, q_L^{\infty}\,(\,\boldsymbol{x}\,)\,, \qquad \forall \boldsymbol{x} \,\in\, \Gamma_1\,,$$

where $k \; \bigl[\,\mathrm{W\,.\,m^{-1}\,.\,K^{-1}}\,\bigr]$ is the thermal conductivity of the wall, $h_L^{\infty} \; \bigl[\,\mathrm{W\,.\,m^{-2}\,.\,K^{-1}}\,\bigr]$ is the surface heat transfer coefficient between the solid material and the surrounding fluid (air) with the temperature $T_L^{\infty} \; \bigl[\,\mathrm{K}\,\bigr]$. The incident flux $q_L^{\infty} \; \bigl[\,\mathrm{W\,.\,m^{-2}}\,\bigr]$ varies with the height of the facade due to the surrounding effects of the urban area and due to the shape of the boundary that may induce local shadings [37]. The surface heat transfer coefficient h_L^{∞} depends on height $y \; \bigl[\,\mathrm{m}\,\bigr]$ and the according wind velocity $v_{\infty} \; \bigl[\,\mathrm{m\,.\,s^{-1}}\,\bigr]$ [38]:

$$h_L^{\infty}\,(\,y\,) \,=\, h_0 \,+\, h_1\,\frac{v_{\infty}}{v_0}\,\Bigl(\frac{y}{y_0}\Bigr)^{\lambda}\,,$$

where $h_0\,,\, h_1 \; \bigl[\,\mathrm{W\,.\,m^{-2}\,.\,K^{-1}}\,\bigr]$ and $\lambda \; \bigl[\,-\,\bigr]$ are given surface coefficients and the velocity variation coefficient respectively. $v_0 \; \bigl[\,\mathrm{m\,.\,s^{-1}}\,\bigr]$ and $y_0 \; \bigl[\,\mathrm{m}\,\bigr]$ are reference quantities.

The right boundary is in contact with the ambient air inside of the building so a ROBIN boundary condition is assumed:

$$k\,\boldsymbol{\nabla} T \cdot \vec{n} \,=\, -\,h_R^{\infty}\,(\,T \,-\, T_R^{\infty}\,)\,, \qquad \forall \boldsymbol{x} \,\in\, \Gamma_3\,,$$

where $T_R^{\infty} \; \bigl[\,\mathrm{K}\,\bigr]$ is the known inside ambient temperature and $h_R^{\infty} \; \bigl[\,\mathrm{W\,.\,m^{-2}\,.\,K^{-1}}\,\bigr]$ is the surface heat transfer coefficient inside the building. Last, the top and bottom boundaries of the facade are assumed as adiabatic:

$$k\,\boldsymbol{\nabla} T \cdot \vec{n} \,=\, 0\,, \qquad \forall \boldsymbol{x} \,\in\, \Gamma_2 \,\cup\, \Gamma_4\,.$$

2.3 Modelling the short wave radiation in the urban environment

The modelling of the radiation received by the boundary Γ_1 is presented. For the detailed mathematical definition, a small element $\mathrm{d}\Gamma_1 \subset \Gamma_1$ of coordinates $\boldsymbol{x} = (x, y, z)$ is considered, as illustrated in Figure 2. The incident short-wave radiation on a tilted surface can be decomposed as follows [39]:

$$q_L^{\infty}(\boldsymbol{x}) = a\left(q^{\mathrm{dr}}(\boldsymbol{x}) + q^{\mathrm{df}}(\boldsymbol{x}) + q^{\mathrm{rf}}(\boldsymbol{x})\right), \tag{2}$$

where direct $q^{\mathrm{dr}}\ [\mathrm{W}\,.\,\mathrm{m}^{-2}]$, diffusive $q^{\mathrm{df}}\ [\mathrm{W}\,.\,\mathrm{m}^{-2}]$ and reflective $q^{\mathrm{rf}}\ [\mathrm{W}\,.\,\mathrm{m}^{-2}]$ fluxes are components of the incident short-wave radiation. a is the absorptivity of the wall.

It is assumed that the environment is modelled as a urban canyon with a front building facing the studied facade as illustrated in Figure 2. As consequence, shadow effects due to the urban environment may affect the direct radiation beam. Furthermore, the varying shape of the facade can induce shadow effects on itself. These effects are considered in the modelling by introducing indicator functions that equals 1 if one has a sunlit boundary. Thus, the direct flux q^{dr} on a titled surface is computed by:

$$q^{\mathrm{dr}}(\boldsymbol{x}) = I_b\, \chi_h(\boldsymbol{x})\, \chi_e(\boldsymbol{x}), \tag{3}$$

where $I_b\ [\mathrm{W}\,.\,\mathrm{m}^{-2}]$ is direct solar density radiation on a titled surface and given by:

$$I_b = I_b^0 \cos(\theta_z)\, r_b,$$

where $I_b^0\ [\mathrm{W}\,.\,\mathrm{m}^{-2}]$ is direct normal incidence solar density radiation, $\theta_z\ [-]$ is the zenith angle, as illustrated in Figure 3, and $r_b\ [-]$ is the beam radiation tilt factor as defined in [40]:

$$r_b = \frac{\cos(\theta_t)}{\cos(\theta_z)},$$

where $\theta_t\ [-]$ is the solar incidence angle, which is the angle between the sun's rays and the normal on a surface, which can be seen on Figure 3. By denoting $\boldsymbol{n} = (n_x, n_y, n_z)$ the outward vector normal to the element $\mathrm{d}\Gamma_1$, tilt angle can be found as following:

$$\cos(\theta_t) = \boldsymbol{s} \cdot \boldsymbol{n},$$

where $\boldsymbol{s} = (s_x, s_y, s_z)$ is the unitary vector defining the solar angle as:

$$\begin{aligned} s_x &= \cos(A_l)\cos(A_z - A_n), \\ s_y &= \cos\left(\frac{\pi}{2} - A_l\right), \\ s_z &= \cos(A_l)\cos\left(\frac{\pi}{2} + A_z - A_n\right), \end{aligned}$$

where $A_l\ [-]$ is the solar altitude angle, $A_z\ [-]$ is the azimuth angle and $A_n\ [-]$ is the Northern hemisphere angle.

Eq. (3) involves χ_h and χ_e the indicator functions due to front building shading and due to self boundary shading, respectively. Then, the indicator function for front building shading is defined as:

$$\chi_h(\boldsymbol{x}) = \begin{cases} 1, & \text{if } y > \mathsf{h}(\boldsymbol{x}), \\ 0, & \text{if } y \leq \mathsf{h}(\boldsymbol{x}). \end{cases} \tag{4}$$

where $\mathsf{h}\ [\mathrm{m}]$ is the height of the projected shadow induced by the front buildings shadow on the boundary Γ_1. It is computed according to:

$$\mathsf{h}(\boldsymbol{x}) = D_y - \frac{D_x + x}{\tan(\theta_z')},$$

where D_x [m] and D_y [m] are the front building distance and height, respectively. Here θ'_z [$-$] is the zenith angle projection on Oxy plane in Figure 2, which can be found as:

$$\theta'_z = \arccos\left(\frac{s_y}{\sqrt{(s_x)^2 + (s_y)^2}}\right).$$

The indicator function (4) equals 1 if the element $\mathrm{d}\Gamma_{1i}$ is higher than the shadow induced by the front buildings. Thus, the element is receiving the incident solar radiation.
The second indicator function involved in Eq. (3) arises from the shadow induced by the shape itself. For this, we consider a second element $\mathrm{d}\Gamma_{1j} \subset \Gamma_1$ of coordinates $\boldsymbol{x}_j = (x_j, y_j, z_j)$, that can induce shadow to the element $\mathrm{d}\Gamma_{1i}$, as illustrated in Figure 2. It is defined by:

$$\chi_{ej}(\boldsymbol{x}, \boldsymbol{x}_j) = \begin{cases} 1, & \text{if } \omega(\boldsymbol{x}, \boldsymbol{x}_j) \neq 0, \\ 0, & \text{if } \omega(\boldsymbol{x}, \boldsymbol{x}_j) = 0, \end{cases}$$

where ω [$-$] is the angle between the unitary vector defining solar angle and the ray created by the two elements:

$$\omega(\boldsymbol{x}, \boldsymbol{x}_j) = \boldsymbol{s} \cdot \boldsymbol{g}_j,$$

where $\boldsymbol{g}_j = (x - x_j, y - y_j, z - z_j)$ is the vector defining ray from one boundary element to another.

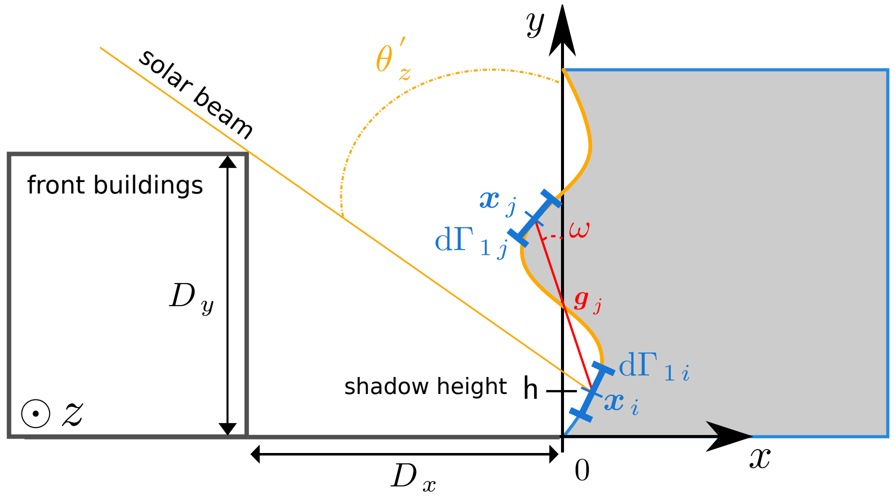

Figure 2. *Illustration of the urban scene and the computation of the shadow effects.*

The indicator function of the whole shape is given by:

$$\chi_e(\boldsymbol{x}) = \min \chi_{ej}, \qquad \forall \boldsymbol{x}_j \in \mathrm{d}\Gamma_j \subset \Gamma_1 \cup \Gamma_4 \setminus \mathrm{d}\Gamma. \tag{5}$$

Thus, if any small element $\mathrm{d}\Gamma_j$ of the whole boundary induces a shadow on the element $\mathrm{d}\Gamma$, then the indicator function returns 0 and the direct solar radiation does not impact such element.

Then, the diffusive flux q^{df} in Eq. (2) is also affected by the shape of the boundary Γ_1. Here the Liu–Jordan model [41] is used for the computations on a tilted surface:

$$q^{\mathrm{df}}(\boldsymbol{x}) = I_d^0 \frac{1}{2}\Big(1 + \cos(\beta(\boldsymbol{x}))\Big),$$

where $I_d^{\,0}\,[\,\mathrm{W\,.\,m}^{-2}\,]$ is the diffuse radiation on a horizontal plane and $\beta\;[\,-\,]$ is the surface tilt angle from the horizontal plane, as illustrated in Figure 3. The angle β is computed by:

$$\cos\,(\,\beta\,(\,\boldsymbol{x}\,)\,)\;=\;\boldsymbol{n}\boldsymbol{\cdot}\boldsymbol{e}_{\,y}\,, \tag{6}$$

with $\boldsymbol{e}_{\,y}\;=\;(0\,,\,1\,,\,0\,)$. Last, the reflective flux $q^{\,\mathrm{rf}}$ in Eq. (2) depends on the intensity of diffuse radiation reflected by the ground and other surfaces surrounding the facade. It is also computed using the Liu–Jordan model [41] according to the orientation of the boundary $\Gamma_{\,1}$:

$$q^{\,\mathrm{rf}}\,(\,\boldsymbol{x}\,)\;=\;\Bigl(I_b^{\,0}\,\sin\Bigl(A_l\Bigr)\,+\,I_d^{\,0}\Bigr)\,\rho\,\frac{1}{2}\Bigl(1\;-\;\cos\,(\,\beta\,(\,\boldsymbol{x}\,)\,)\Bigr)\,, \tag{7}$$

where $\rho\,[\,-\,]$ is albedo of the surrounding environment.

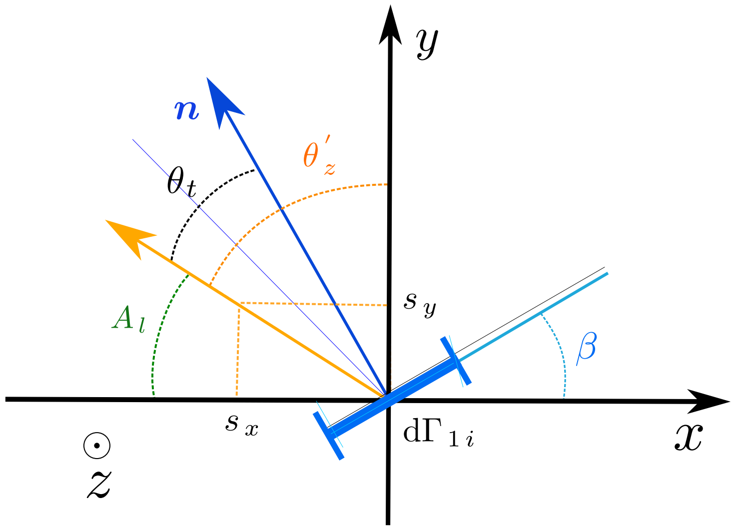

Figure 3. *Solar angles diagram.*

2.4 Dimensionless formulation

The space, time and temperature quantities are transformed into a dimensionless representation according to:

$$\boldsymbol{x}^{\,\star}\;=\;(\,x^{\,\star}\;,\,y^{\,\star}\,)\,,\qquad x^{\,\star}\;=\;\frac{x}{H}\,,\qquad y^{\,\star}\;=\;\frac{y}{H}\,,\qquad u\;=\;\frac{T}{T_\infty}\,.$$

With this transformations, the dimensionless problem is set on the new domain $\Omega^{\,\star}$ and the left boundary Γ_1 is now redefined as:

$$\Gamma_1^{\star}(\boldsymbol{p}^{\star}\,)\;=\;\{\,\boldsymbol{x}^{\,\star}\,|\;x^{\,\star}\;=\;\gamma^{\star}\,(\,\boldsymbol{p}^{\star}\,,\,y^{\star}),\,y^{\star}\;\in\;[\,0\,,\,1\,]\,,\,\boldsymbol{p}^{\star}\;\in\;\Omega_p^{\star}\}\,.$$

Then, the governing equations is:

$$\boldsymbol{\Delta}^{\,\star}\,u\;=\;0\,, \tag{8}$$

with the boundary conditions:

$$\begin{aligned}
\nabla^{\,\star}\,u\boldsymbol{\cdot}\vec{n}\;&=\;-\,\mathrm{Bi}_L(\boldsymbol{x}^{\star})\cdot(\,u\;-\;u_L^{\infty})\;+\;\rho(\boldsymbol{x}^{\,\star})\,, && \boldsymbol{x}^{\,\star}\in\Gamma_{\,1}\,,\\
\nabla^{\,\star}\,u\boldsymbol{\cdot}\vec{n}\;&=\;0\,, && \boldsymbol{x}^{\,\star}\in\Gamma_2\,\cup\,\Gamma_{\,4}\,,\\
\nabla^{\,\star}\,u\boldsymbol{\cdot}\vec{n}\;&=\;-\,\mathrm{Bi}_R\,(\,u\;-\;u_R^{\infty})\,, && \boldsymbol{x}^{\,\star}\;\in\;\Gamma_3\,,
\end{aligned}$$

where $\rho(\boldsymbol{x}^\star)$ is the dimensionless incident flux, Bi_L and Bi_R are BIOT numbers, which are equal to:

$$\rho(\boldsymbol{x}^\star) \;=\; \frac{q_L^{\infty}\,(\,\boldsymbol{x}^\star\,)\,H}{k\,T_\infty}\,, \quad \mathrm{Bi}_L(\,\boldsymbol{x}^\star\,) \;=\; \frac{h_L^{\infty}\,(\,\boldsymbol{x}^\star\,)\,H}{k}\,, \quad \mathrm{Bi}_R \;=\; \frac{h_R^{\infty}\,H}{k}\,.$$

The methodology is described for dimensionless variables, thus for the sake of clarity the symbol $\star$ will be later omitted in this section.

2.5 Numerical method to solve the direct problem

2.5.1 Boundary Integral equation

To derive the boundary integral equation of Eq. (8), we use GREEN's second identity for two regular functions:

$$\int_{\Omega\,-\,\Omega\epsilon} \Big(\,u\,\nabla^2\,\Phi \;-\; \Phi\,\nabla^2\,u\,\Big)\,dV \;=\; \int_{\Gamma} \Big(\,u\,q^{\,*} \;-\; \Phi\,q\,\Big)\,d\Gamma \,+\, \int_{\Gamma_\epsilon} \Big(\,u\,q^{\,*} \;-\; \Phi\,q\,\Big)\,d\Gamma_\epsilon, \qquad (9)$$

where u is solution of our dimensionless problem defined for the bounded two-dimensional region Ω with its closed boundary curve Γ. Φ is the fundamental solution of LAPLACE's equation for the bounded two-dimensional region $\Omega_{\,\epsilon}$ with its closed boundary curve $\Gamma_{\,\epsilon}$. q and q^* are normal derivatives for u and Φ:

$$\begin{aligned} q \;&=\; \nabla\,u\cdot\vec{n}, \\ q^{\,*} \;&=\; \nabla\,\Phi\cdot\vec{n}. \end{aligned}$$

Last, Φ is defined by :

$$\Phi \;=\; -\,\frac{\ln\,(\,r\,)}{2\,\pi},$$

where r is the distance from a source point to a boundary point, which is defined as:

$$r \;=\; \Big[\,(\,x \;-\; x_\xi)^2 \;+\; (\,y \;-\; y_\xi)^2\,\Big]^{1/2},$$

here $\boldsymbol{x}_{\,\xi} \;=\; (\,x_\xi\,,\,y_\xi\,)$ is a source point coordinates and $\boldsymbol{x} \;=\; (x,\,y)$ is a boundary point coordinates, which is shown in Figure 4(a).

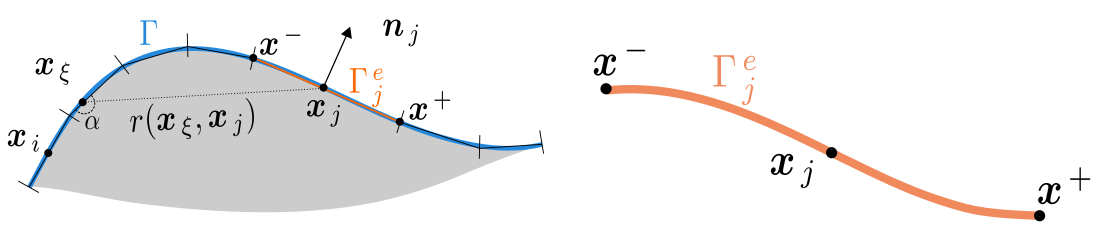

(a) (b)

Figure 4. *Illustration of the approximation of the whole boundary* Γ (a) *and of one boundary element* $\Gamma_{\,j}$ (b)*.*

u and Φ satisfy LAPLACE's equation in the new region $\Omega \;-\; \Omega\epsilon$, thus the domain integral is equal to zero. The original region is recovered on taking the limit when $\epsilon \,\rightarrow\, 0$. The limit of the second integral on the right-hand side over Γ_ϵ in Eq. (9) produces the result:

$$\lim_{\epsilon\,\rightarrow\,0} \int_{\Gamma_\epsilon} \Big(\,u\,(\boldsymbol{x})\,q^{\,*}(\boldsymbol{x}_{\,\xi},\,\boldsymbol{x}) \;-\; \Phi(\boldsymbol{x}_{\,\xi},\,\boldsymbol{x})\,q\,(\boldsymbol{x})\,\Big)\,d\Gamma_\epsilon \;=\; u(\boldsymbol{x}_{\,\xi})\,,$$

and the following integral equation is obtained from Eq. (9):

$$u(\boldsymbol{x}_\xi) \;=\; \int_\Gamma \Big(\Phi(\boldsymbol{x}_\xi,\, \boldsymbol{x})\, q\,(\boldsymbol{x}) \;-\; u\,(\boldsymbol{x})\, q^*(\boldsymbol{x}_\xi,\, \boldsymbol{x})\Big)\, d\Gamma, \tag{10}$$

this equation is known as Green's third identity.

To obtain a boundary integral equation relating only boundary values, the limit is taken when the point $\boldsymbol{x}_\xi$ tends to a point $\boldsymbol{x}$ on the boundary Γ. However, if $\boldsymbol{x}_\xi$ belongs to the boundary Γ. The limits produce what is called a free term. Taking into account these terms the boundary integral equation Eq. (10) can be generalized in the form:

$$c(\boldsymbol{x}_\xi)\, u(\boldsymbol{x}_\xi) \;=\; \int_\Gamma \Big(\Phi(\boldsymbol{x}_\xi,\, \boldsymbol{x})\, q\,(\boldsymbol{x}) \;-\; u\,(\boldsymbol{x})\, q^*(\boldsymbol{x}_\xi,\, \boldsymbol{x})\Big)\, d\Gamma, \tag{11}$$

for any point $\boldsymbol{x}_\xi$ on the boundary Γ. The free coefficient $c(\boldsymbol{x}_\xi)$ is given by:

$$c(\boldsymbol{x}_\xi) \;=\; \frac{\alpha}{2\,\pi}, \qquad 0 \le c(\boldsymbol{x}_\xi) \le 1,$$

where α is an internal angle at source point $\boldsymbol{x}_\xi$.

2.5.2 Discrete Boundary Integral equation

The Boundary integral equation (BIE) Eq. (11) can only be solved analytically for some very simple problems. For this, a standard Green's function method is normally used [42]. Rather than attempting analytical solutions to the BIE for particular geometries and boundary conditions, we seek a suitable reduction of the equation to an algebraic form that can be solved by a numerical approach.

The Boundary element method (BEM) is a numerical method of solution of the BIE, based on a discretization procedure [43]. Application requires two types of approximation: the first geometrical, involving a subdivision of the boundary Γ into N_e small segments or elements Γ_j, schematically shown in Figure 4(b), such that:

$$\sum_{j=1}^{N_e} \Gamma_j \approx \Gamma,$$

Taking this into account, Eq. (11) can be written in the form:

$$c(\boldsymbol{x}_\xi)\, u(\boldsymbol{x}_\xi) \;=\; \sum_{j=1}^{N_e} \int_{\Gamma_j} \Big(\Phi(\boldsymbol{x}_\xi,\, \boldsymbol{x})\, q\,(\boldsymbol{x}) \;-\; u\,(\boldsymbol{x})\, q^*(\boldsymbol{x}_\xi,\, \boldsymbol{x})\Big)\, d\Gamma, \tag{12}$$

The second approximation required by the BEM is functional. We approximate the variation of u and q within each element by writing them in terms of their values at some fixed points in the element (nodal points or nodes), using interpolation functions.

The simplest possible approximation is a piecewise constant one, which assumes that u and q are constant within each element and equal to their value at the midpoint. Using this approximation into Eq. (12), we obtain:

$$c(\boldsymbol{x}_i)\, u(\boldsymbol{x}_i) \;=\; \sum_{j=1}^{N_e} q\,(\boldsymbol{x}_j) \int_{\Gamma_j} \Phi(\boldsymbol{x}_i,\, \boldsymbol{x})\, d\Gamma \;-\; u\,(\boldsymbol{x}_j) \int_{\Gamma_j} q^*(\boldsymbol{x}_i,\, \boldsymbol{x})\, d\Gamma, \tag{13}$$

here i - nodal point, j - number of the element, note that $q\,(\boldsymbol{x}_j) \;=\; \nabla\, u(\boldsymbol{x}_j)\; \vec{n}_j$ and $q^*(\boldsymbol{x}_i,\, \boldsymbol{x}) \;=\; \nabla\, \Phi(\boldsymbol{x}_i,\, \boldsymbol{x})\; \vec{n}_i$. Note that for the piecewise constant elements boundary is smooth which means the free term $c(\boldsymbol{x}_i)$ is equal to $\frac{1}{2}$.

Calling integrals

$$G_{ij} = \int_{\Gamma_j} \Phi(\boldsymbol{x}_i, \boldsymbol{x})\, d\Gamma \tag{14}$$

and

$$H_{ij} = \int_{\Gamma_j} q^*(\boldsymbol{x}_i, \boldsymbol{x})\, d\Gamma + c(\boldsymbol{x}_i)\, \delta_{ij}, \tag{15}$$

where δ_{ij} is the KRONECKER delta:

$$\delta_{ij} = \begin{cases} 1, & \text{if } i = j, \\ 0, & \text{if } i \neq j. \end{cases} \tag{16}$$

2.5.3 Numerical integration

Integration in Eq. (14) and (15) is carried out using composite SIMPSON's rule. Quadratic boundary elements are used to represent curved geometry. They provide increased accuracy because of their better representation of the variation of the functions along the boundary. The variation of coordinates $\boldsymbol{x}$ within each quadratic element is defined by their values at three global nodal points $\boldsymbol{x}^-$, $\boldsymbol{x}^o$, $\boldsymbol{x}^+$ using suitable interpolation functions, which are function of the homogeneous coordinate η:

$$\boldsymbol{x}(\eta) = N_1 \boldsymbol{x}^- + N_2 \boldsymbol{x}^o + N_3 \boldsymbol{x}^+,$$

with

$$N_1 = \frac{1}{2}\eta(\eta - 1), \qquad N_2 = (1 - \eta^2), \qquad N_3 = \frac{1}{2}\eta(\eta + 1),$$

η is the dimensionless coordinate varying $-1 \leq \eta \leq 1$. The difference with the numerical implementation of quadratic elements is that the Jacobian and normal vector are no longer constant within each element. In order to implement them, there is a need to transform from Cartesian to curvilinear coordinates [44]. The transformation from $d\Gamma$ to $d\eta$ is now given by:

$$d\Gamma = |J|\, d\eta,$$

with the Jacobian computed in the form:

$$|J| = \sqrt{J_x^2 + J_y^2} = \frac{d\Gamma}{d\eta},$$

in which

$$J_x = \frac{dx}{d\eta}, \qquad J_y = \frac{dy}{d\eta}.$$

Hence one can write for Eq. (14):

$$G_{ij} = \int_{-1}^{1} \Phi\Big(\boldsymbol{x}(\eta_i), \boldsymbol{x}(\eta)\Big)\, |J|\, d\eta.$$

Similarly, other integrals can be computed. The components of the unit normal vectors at any point are given by:

$$n_x = \frac{J_y}{|J|}, \qquad n_y = -\frac{J_x}{|J|}.$$

2.5.4 Computation of temperatures and fluxes

After computation of integrals Eq. (13) can be rewritten in the form:

$$\sum_{j=1}^{N_e} H_{i\,j}\, u_j \;=\; \sum_{j=1}^{N_e} G_{i\,j}\, q_j, \tag{17}$$

for any nodal point i. If the above equations are now applied, this generates a system of equations which can be written in matrix form as:

$$\underline{\underline{\boldsymbol{H}}}\,\underline{\boldsymbol{u}} \;=\; \underline{\underline{\boldsymbol{G}}}\,\underline{\boldsymbol{q}}\,. \tag{18}$$

If the boundary conditions of the problem are a combination of prescribed temperature and prescribed fluxes, the system of Eq. (18), the matrices can be reordered and solved in the form:

$$\underline{\underline{\boldsymbol{A}}}\,\underline{\boldsymbol{x}} \;=\; \underline{\boldsymbol{b}}\,, \tag{19}$$

in which all unknowns have been collected into the vector $\underline{\boldsymbol{x}}$, and the vector $\underline{\boldsymbol{b}}$ is the 'load' vector, which contains all known boundary conditions. However, if the boundary condition at all surfaces are of the convective type $q \;=\; -\,\mathrm{Bi}\,(\,u \;-\; u^{\,\infty}\,)$, $\underline{\boldsymbol{q}}$ needs to be applied at all boundary nodes:

$$\underline{\underline{\boldsymbol{q}}} \;=\; \underline{\underline{\boldsymbol{D}}}\,\underline{\boldsymbol{u}} \;+\; \underline{\boldsymbol{E}}\,, \tag{20}$$

where the diagonal matrix $\underline{\underline{\boldsymbol{D}}}$ and the vector $\underline{\boldsymbol{E}}$ contain the values of $(-\mathrm{Bi})$ and $(\mathrm{Bi}\,u^{\,\infty})$, respectively, at each boundary node. Substituting Eq. (20) into Eq. (18) yields the system of equations:

$$(\underline{\underline{\boldsymbol{H}}} \;-\; \underline{\underline{\boldsymbol{G}}}\,\underline{\underline{\boldsymbol{D}}})\,\underline{\boldsymbol{u}} \;=\; \underline{\underline{\boldsymbol{G}}}\,\underline{\boldsymbol{E}}\,, \tag{21}$$

which can be solved for the boundary values of temperature. Heat fluxes along the boundary may then be evaluated pointwise by using the boundary condition Eq. (20).

3 Design optimization problem

The objective of this work is to improve energy efficiency of a building wall by finding the optimal shape of the left boundary $\Gamma_{\,1}$ which is in contact with outside environment. In general, heat transfer design objectives can be classified into two categories: *(i)* heat transfer augmentation problems and *(ii)* thermal insulation problems. Thus, the optimization problem aims at finding parameters of the left boundary that minimizes the entropy generation rate on the right wall:

$$\boldsymbol{p}^{\,\circ} \;=\; \arg\min_{\boldsymbol{p}\,\in\,\Omega_{\,p}} \mathcal{J}\,(\,\boldsymbol{p}\,)\,. \tag{22}$$

The objective function $\mathcal{J}\;\bigl[\,\mathrm{W\,.\,m}^{\,-2}\,\bigr]$ is the total inward heat flux on the right boundary, corresponding to the inside of the building:

$$\mathcal{J}\,(\,\boldsymbol{p}\,) \;=\; \sigma\int_{0}^{H} -k\,\boldsymbol{\nabla}\,T\;(\,\gamma\,(\,\boldsymbol{p}\,,\,y)\,)\;\vec{n}\,dy\,, \tag{23}$$

where σ is the parameter which takes values -1 and 1. In other words the first case requires the highest thermal conductance for the heat transfer augmentation. Consequently, in the second case the thermal conductance is the lowest for the thermal insulation problems.

Note that the objective function needs to be optimized under several constraints. First, the physical area of the wall $S\,(\,\boldsymbol{p}\,)$ should not exceed the reference case area S_{∞}. The reference case is defined as the flat standard wall ($\gamma = 0$ in Eq. (1)). Thus, the cost function Eq. (23) needs to be optimized under the following constraint:

$$S(\boldsymbol{p}) \leq S_\infty,$$

which leads to given the representation in Figure 1

$$\int_{\Gamma_3} L\, d\Gamma - \int_{\Gamma_1} \gamma(\boldsymbol{p}, y)\, d\Gamma \leq \int_{\Gamma_3} L\, d\Gamma,$$

which can be rewritten as

$$\int_{\Gamma_1} \gamma(\boldsymbol{p}, y)\, d\Gamma \geq 0. \tag{24}$$

The second constraint that must be satisfied by the parametrized mapping is that the maximum width of the wall cannot be higher than L. In other words, the left and right boundaries cannot overlap:

$$\gamma(\boldsymbol{p}, y) \leq L - \delta, \tag{25}$$

where δ is a given spatial tolerance.

The extremums of cost function Eq. (23) are found with brute-force search [45]. The objective function is evaluated at a finite number of parameters within a specified constrained domain. In this article each parameter in the domain is uniformly discretized for ten values.

4 Verification of the numerical model

4.1 Shortwave radiation model

First, a reference solution is considered to verify proposed shortwave radiation model. The reference solution is obtained using pixel counting technique [46]. The method for the reference is chosen due to a number of advantages over the methods used by most building energy simulation software today [47, 48]. The pixel counting method handles complex shape models with large numbers of surfaces and curved geometries, which can take into account shading by surrounding buildings and self-shading structures. In this work the pixel counting technique cannot be utilized since its' coupling with the direct model and the optimization strategy faces some technical issues.

Verification case study considers building facade wall in contact with incidence short-wave radiation on December 21 from 9 h. to 17 h. in Marseille city, France. The height of the wall is $H = 3\,\mathrm{m}$. For the mapping function γ in Eq. (1), a sine function is considered:

$$\gamma(\boldsymbol{p}, y) = 0.2 \sin(\pi y),$$

which is shown on Figure 5(a). The urban environment assumes a front building of $D_y = 3$ m height and placed at $D_x = 4.76$ m of the boundary Γ_1. The absorptivity of the right boundary and the albedo of the surrounding environment are set to $a = 0.5$ and $\rho = 0.2$. The Northern hemisphere angle is $A_n = 2\pi$. Zenith angle θ_z, direct normal incidence solar density radiation I_b^0, diffuse radiation on a horizontal plane I_d^0, solar altitude A_l and azimuth A_z angles values are given in Table 1 with respect to time.

In order to illustrate the relative mean square error between proposed model and pixel counting technique following formula is used:

$$\varepsilon_{2,r} \circ f = \frac{||f - \hat{f}||_2}{||\hat{f}||_2} \cdot 100\%,$$

Table 1. *Input parameters for validation of SWR.*

$t\,[\mathrm{h}]$	$\theta_z\,[-]$	$I_b^0\,[\mathrm{W\,.\,m^{-2}}]$	$I_d^0\,[\mathrm{W\,.\,m^{-2}}]$	$A_l\,[-]$	$A_z\,[-]$
9	83.22	0.0	16.0	6.66	131.46
10	75.91	91.0	72.0	14.03	143.27
11	70.45	139.0	138.0	19.50	156.46
12	67.39	186.0	176.0	22.57	170.82
13	67.06	253.0	172.0	22.90	185.74
14	69.51	386.0	138.0	20.44	200.30
15	74.46	417.0	104.0	15.49	213.79
16	81.39	304.0	73.0	8.50	225.92
17	89.51	10.0	27.0	0.01	236.77

where f represents solution obtained by proposed model and $\hat{f}$ is the reference solution. Calculated results are satisfactory and consistent with the pixel counting estimations. Figure 5(b) shows error at each hour for the wall shape at Figure 5(a). Note that, it scales with 10^{-1}, which means error doesn't exceed 1 %. In addition, for the different incident short-wave radiation components, Figure 6 illustrates the comparison of both model at $t = \{9\,,\,12\,,\,15\}$ h, respectively. It shows a good agreement between both approaches.

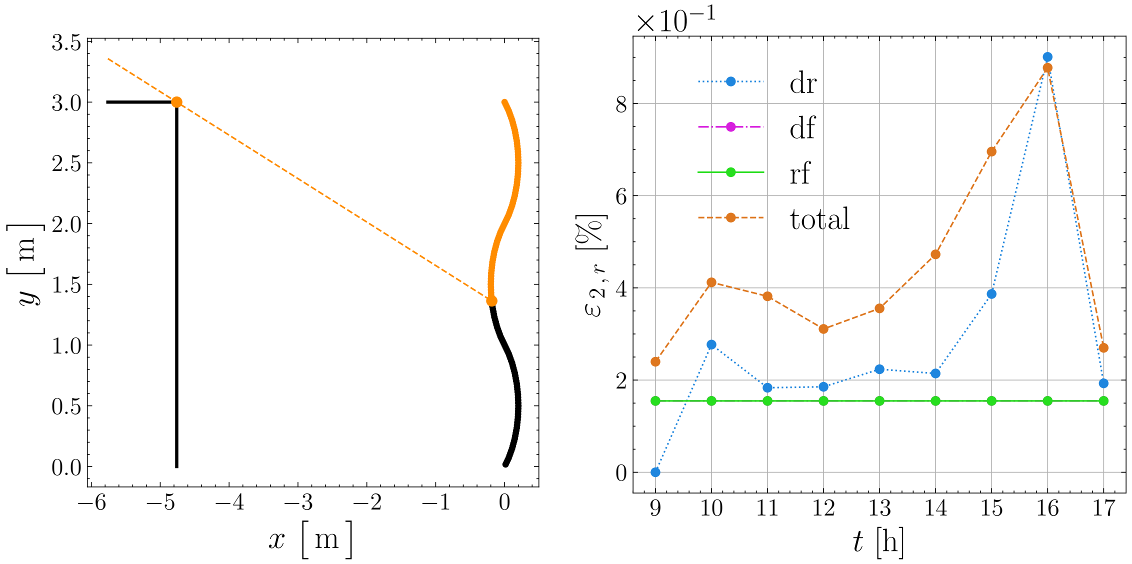

(a) (b)

Figure 5. *Shape of the wall for SWR comparison* (a) *and* ε_2 *error of* q^{dr} *direct,* q^{df} *diffusive and* q^{rf} *reflective fluxes with reference results during one day* (b).

4.2 BEM numerical model

Analytical solution $\hat{u}$ for Eq. (8) is used as a reference for verification of numerical solutions:

$$\hat{u}\,(\boldsymbol{x}) \;=\; x^{\,2} \;-\; y^{\,2}. \tag{26}$$

The boundary conditions will be in the following sections. The verification will be carried for two cases: rectangular and non-rectangular domains. The latter is defined by a third order

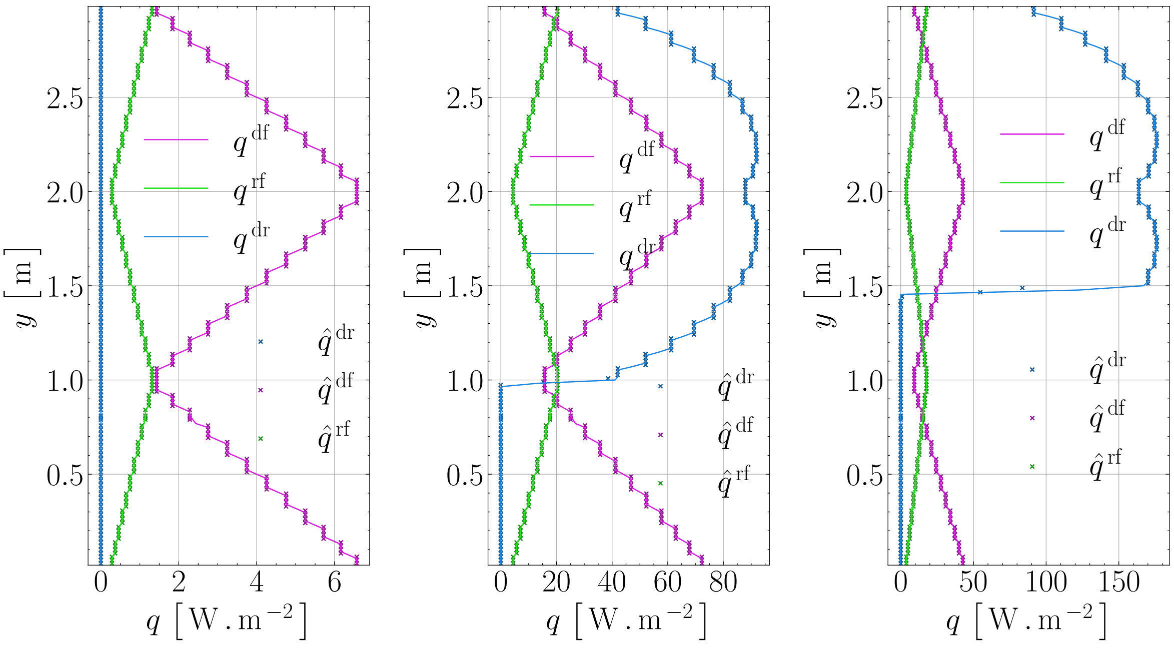

(a) (b) (c)

Figure 6. *Comparison of* q^{dr} *direct,* q^{df} *diffusive and* q^{dr} *reflective fluxes with reference results at 9h, 12h and 15h.*

polynomial function. The purpose is to verify the BEM model for a case relatively close to ones that will be investigated for thermal design.

4.2.1 Rectangular domain

Firstly, the BEM is verified on a rectangular domain with the $L = 0.75$ and $H = 1$. Thus, it corresponds to a flat facade with mapping function $\gamma(\boldsymbol{P}, y) = 0$. Since the objective of this work lies on computation of fluxes on boundaries, the following boundary conditions are considered for the problem Eq. 8:

$$\begin{aligned}
u &= -y^{2}, && \forall \boldsymbol{x} \in \Gamma_{1}, \\
u &= x^{2}, && \forall \boldsymbol{x} \in \Gamma_{2}, \\
u &= L^{2} - y^{2}, && \forall \boldsymbol{x} \in \Gamma_{3}, \\
u &= x^{2} - H^{2}, && \forall \boldsymbol{x} \in \Gamma_{4}.
\end{aligned}$$

To compute analytical solution $\hat{q}\,(\boldsymbol{x})$ for fluxes on boundaries, one has to take normal derivatives of $\hat{u}$. The analytical solution is compared with the BEM as well as the finite-difference method (FDM). The latter is implemented using Gauss-Seidel's method. For the numerical solution output u, the error ε_{2} is computed according to:

$$\varepsilon_{2} \circ u = \big|\big|\, u - \hat{u} \,\big|\big|_{2},$$

where $\hat{u}$ is reference solution. The fluxes q are computed for all boundary points. Different values of the spatial step Δh are chosen according to the total number of boundary elements N_{e}.

Figure 7(a) presents the error according the spatial step of each method. It highlights that BEM results has a significant lower error compared to FDM results for all spatial step. BEM approach has an error behaviour between $\mathcal{O}(\Delta h)$ and $\mathcal{O}(\Delta h^{2})$ in contrast with FDM approach, which has first order behaviour. Figure 7(b) gives the computational time ratio according to the error. Here, the ratio is computed so that the maximal value is one for the method that requires the most computational resources. The Figure shows that with the decreasing number of spatial step computational time is similar for both methods, however the BEM approach shows better accuracy.

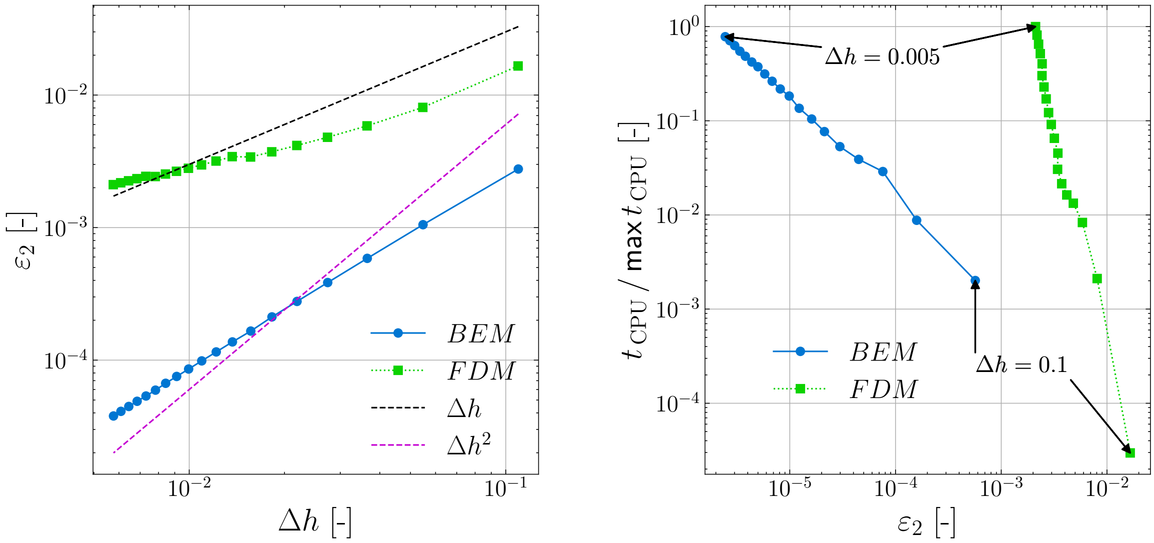

(a)

(b)

Figure 7. *Influence of spatial step* Δh *on* ε_2 *error for dimensionless* q (a) *and on the ratio* t_{CPU} *time and* ε_2 (b) ($\max\, t_{CPU} = 157.42\,\mathrm{s}$).

4.2.2 non-rectangular domain

Secondly, the BEM approach is verified on a non-rectangular domain with the same spacial parameters L and H as in rectangular case. A third order polynomial function is considered for the mapping function γ as shown in Figure 8(a):

$$\gamma(\boldsymbol{p}, y) = p_0\, y\, (y - p_1)(y - 1).$$

Mapping function's parameters are set to $p_0 = 3$ and $p_1 = 0.5$. Boundary conditions are considered same as in previous case except for Γ_1 due to the varying shape:

$$u = x^2 - y^2, \qquad \forall\, \boldsymbol{x} \in \Gamma_1,$$

As in case of rectangular shape, same analyse is conducted. However, the BEM is compared only with analytical solution from Eq. 26. Figure 8(b) shows error variation according to the spatial step Δh. Similarly to previous rectangular case, the BEM error increase according to slope between first and second orders.

5 Case study: improving the thermal efficiency of a building facade

Since the shortwave radiation model and the BEM numerical method have both been verified, a real case study is now investigated for improving the thermal design of a building facade. First,

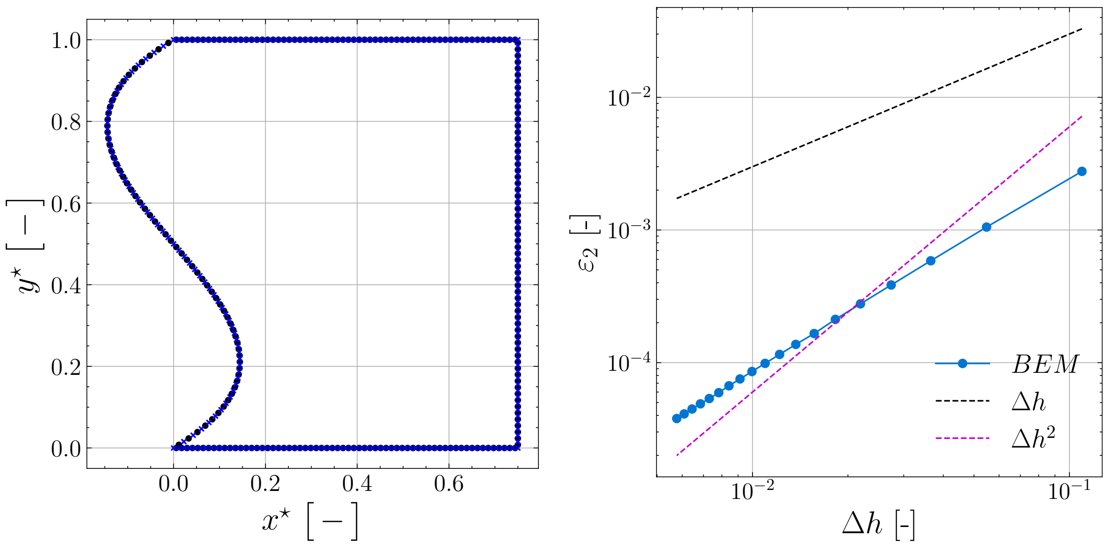

(a)

(b)

Figure 8. *Influence of spatial step* Δh *on* ε_2 *error for dimensionless* q (b) *in case of nonlinear wall shape* (a)*.*

description of case study is given to show physical properties of house wall under consideration. Second, the influence of the sunlit is analysed after preliminary numerical experiments. Third, two solstice days are chosen for numerical investigations according to heat transfer objectives. Fourth, after achieving improved wall shapes for both cases similar investigations are made for whole year period.

5.1 Description

Case study considers a house wall under different climate conditions over the year. Sky is considered clear, with no clouds. The wall is composed of a cement mortar with thermal conductivity $k = 1\,\mathrm{W\,.\,m^{-1}\,.\,K^{-1}}$ [49]. The height and width of the wall are $H = 3\,\mathrm{m}$ and $L = 0.3\,\mathrm{m}$. The absorptivity of the right boundary is set to $a = 0.5$. The incident radiation flux are computed using analytical projections of the solar angle, considering shadow induced by front building and by the own shape of the boundary Γ_1. For the boundary Γ_1, initial coefficients are taken as $h_0 = 5.82\ \left[\mathrm{W\,.\,m^{-2}\,.\,K^{-1}}\right]$, $h_1 = 3.96\ \left[\mathrm{W\,.\,m^{-2}\,.\,K^{-1}}\right]$, $\lambda = 0.32$, $v_0 = 1\ \left[\mathrm{m\,.\,s^{-1}}\right]$, $y_0 = 65.33\ \left[\mathrm{m}\right]$.

5.2 Preliminary results: influence of the sunlit

According to our numerical experiments, facade shape can be improved from reference (flat wall) case only for cases when wall has sunlit regions on its' surface. In other words, optimization depends on position of neighbour building (distance D_x and height D_y) and the day of the year, which is zenith angle projection ($\theta_z^{'}$) of the sun. From this preliminary analysis, optimization for two cases of *(i)* heat transfer augmentation and *(ii)* thermal insulation problems (See Section 3) is proposed for Nice city, France.

In case of the heat transfer augmentation problem wall surface has to be fully or partially under sunlit, which domain is depicted with grey color on Figure 9(a). For instance in Figure 9(a) red "star" marker represent December 21^{st} at noon with $\theta_z^{'} = 68.88^\circ$ and $\frac{D_x}{D_y} = 0.8$. Since red "star" is in the grey area, one can improve facade design. Contrarily black "plus" marker represent February 1^{st} with $\theta_z^{'} = 62.10^\circ$ and $\frac{D_x}{D_y} = 0.3$, one can not improve the thermal facade design.

In case of the thermal insulation problems facade has to be partially under sunlit, which domain is illustrated with grey color on Figure 9(b). First, red "star" marker represent June 21^{st} at noon with $\theta_z^{'} = 18.69^\circ$ and $\frac{D_x}{D_y} = 0.27$. Since red "star" is in the grey area, one can have shape optimization. Additionally one could already deduced Figure 9 shows us variation of the $\theta_z^{'}$ in Nice according to seasons of the year, which is shown by different color regions.

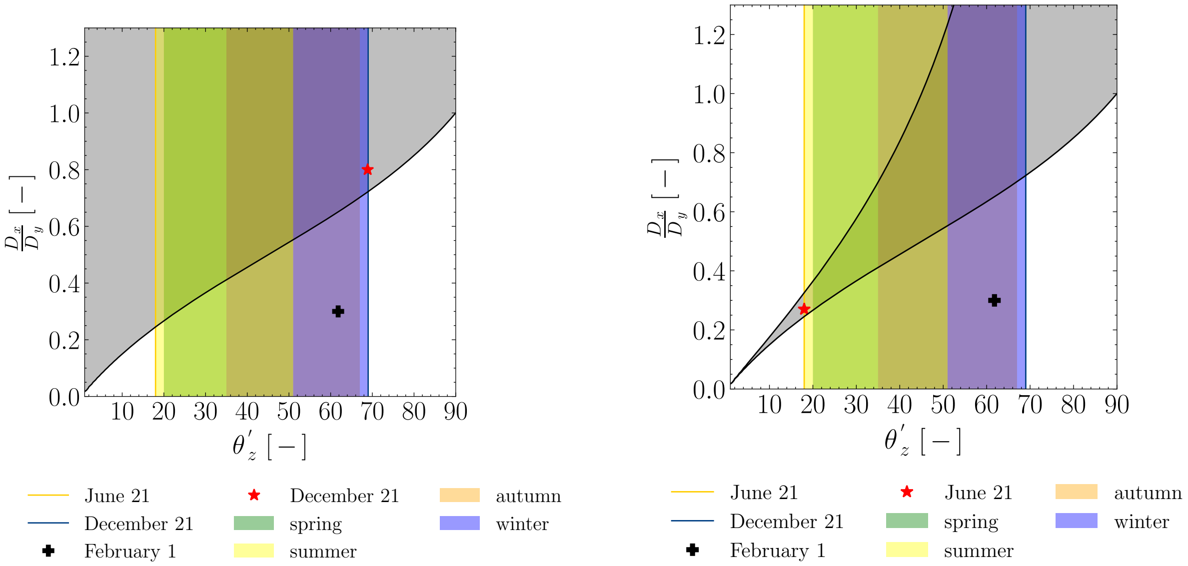

(a)

(b)

Figure 9. *Shape optimization domains (grey color) for heat transfer augmentation* (a) *and thermal insulation* (b) *design objectives with respect to the ratio* $\frac{D_x}{D_y}$ *on zenith angle projection* $\theta_z^{'}$.

5.3 Results for solstice days

The number of boundary elements is set to $N_e = 256$. The spatial tolerance is set to $\delta = 0.25\,L$. As mentioned before the urban environment assumes a front building placed on different positions with the height $D_y\ [\,\mathrm{m}\,]$ and distance $D_x\ [\,\mathrm{m}\,]$ of the boundary Γ_1. For the mapping function γ Eq. (1), a third order polynomial is considered:

$$\gamma\,(\,\boldsymbol{p}\,,\,y\,) = p_0\,y\left(\frac{y}{H} - p_1\right)\left(\frac{y}{H} - 1\right) - \frac{H\,p_0}{12}\,(\,2\,p_1 - 1\,)\,.$$

With such equation, parameter p_0 states the convexity of the shape and p_1 the roots of the equation, *i.e.* it regulates the total area of the facade. As described in Section 3, area and boundary constraints (Eq. (24) and Eq. (25)) have to be satisfied. Application of constraints for mapping function is demonstrated in Appendix A. As a result, we have:

$$p_1 \in [\,0\,,\,1\,]\,, \qquad \hat{p}_0^{-}\,(\,p_1\,) \leq p_0 \leq \hat{p}_0^{+}\,(\,p_1\,)\,,$$

with expression of $\hat{p}^{-}$ and $\hat{p}^{+}$ given by Eq. (32) in Appendix A. The parameters domain is illustrated in Figure 10(a). Note that it is a connected space. After preliminary analysis using exhaustive search method the objective function distribution is shown in Fig. 10(b) for December 21^{st} at noon.

The shape optimization is carried out for two dates (December 21^{st} and June 21^{st}). December 21^{st} is chosen for heat transfer augmentation problem, since it aims to increase the rate of heat transfer in winter period. Contrary, June 21^{st} is considered for thermal insulation problem, since

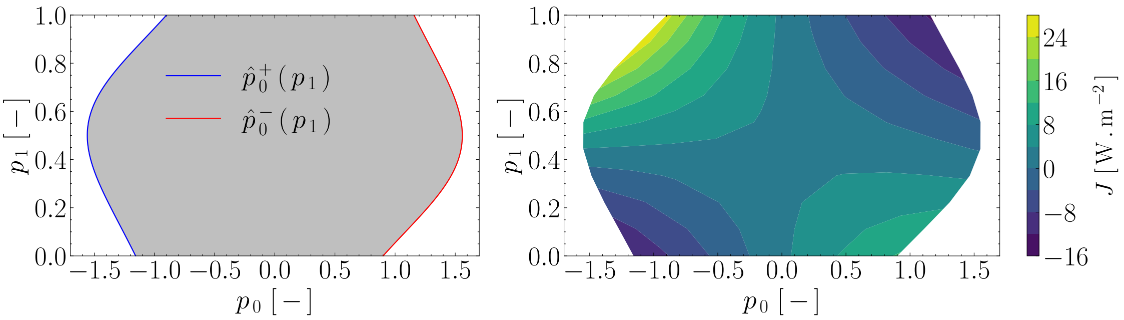

(a)

(b)

Figure 10. *Domain of* $\boldsymbol{p}$ *variation* (a) *and the distribution of the objective function value in the domain resulting from the exhaustive search* (b) *on December 21*st *at noon.*

it aims to reduce heat transfer in summer period. According to irradiation weather data filed taken from Meteonorm [50], climatic data are provided in Table 2.

Table 2. *Input parameters for case study.*

Day	T_R $[\mathrm{K}]$	T_L $[\mathrm{K}]$	v_∞ $[\mathrm{m\,.\,s^{-1}}]$	θ_z	I_b^0 $[\mathrm{W\,.\,m^{-2}}]$	I_d^0 $[\mathrm{W\,.\,m^{-2}}]$	A_l	A_z
December 21st	292.15	285.06	4.0	70.30	726.64	95.73	19.70	202.07
June 21st	297.15	296.86	4.0	27.05	640.38	237.21	62.95	228.51

First analysis focuses on the heat transfer augmentation problem on December 21st. The reference $\boldsymbol{p}_{ref}$ and optimized $\boldsymbol{p}^\circ$ parameters are given in Table 3. The neighbor building height and distance are given by proportion $\frac{D_x}{D_y}$. The reference flat wall and the optimized one are illustrated in Figure 11 with the corresponding short wave radiation distribution. The heat transfer is increased by 800%. Figure 11(d) reveals that it is achieved due to concavity on the top of the wall and convexity on the bottom, which lead to higher influence of short wave radiation. In addition to that, Table 4 shows optimization results for December 21st at noon for the different heat conductivity k and height H values of the facade. When thermal conductivity varies, with height remaining constant, the optimized shape parameters p_0° and p_1° remain the same. Contrariwise, when height changes and thermal conductivity is constant, the optimized shape of the wall is modified. It confirms our preliminary analyse indicating that the optimization procedure depends mainly on the sunlit on the facade, driven by geometrical parameters such as height, front building distance and height.

Table 3. *Optimization results.*

	Cost function value		Optimized shape parameter		Neighbour building
Day	$\mathcal{J}(\boldsymbol{p}_{ref})$	$\mathcal{J}(\boldsymbol{p}^\circ)$	p_0°	p_1°	$D_x\,/\,D_y$
heat transfer augmentation problems					
December 21st	3.17	26.39	−1.11	0.89	0.8
thermal insulation problems					
June 21st	69.26	60.61	−0.70	0.0	0.27

Second analysis deals with thermal insulation problem on June 21st. Results are presented in Table 3. The optimized shape is depicted in Figure 12 with the corresponding short wave radiation distribution. Obtained results show benefits for energy efficiency. The heat transfer is

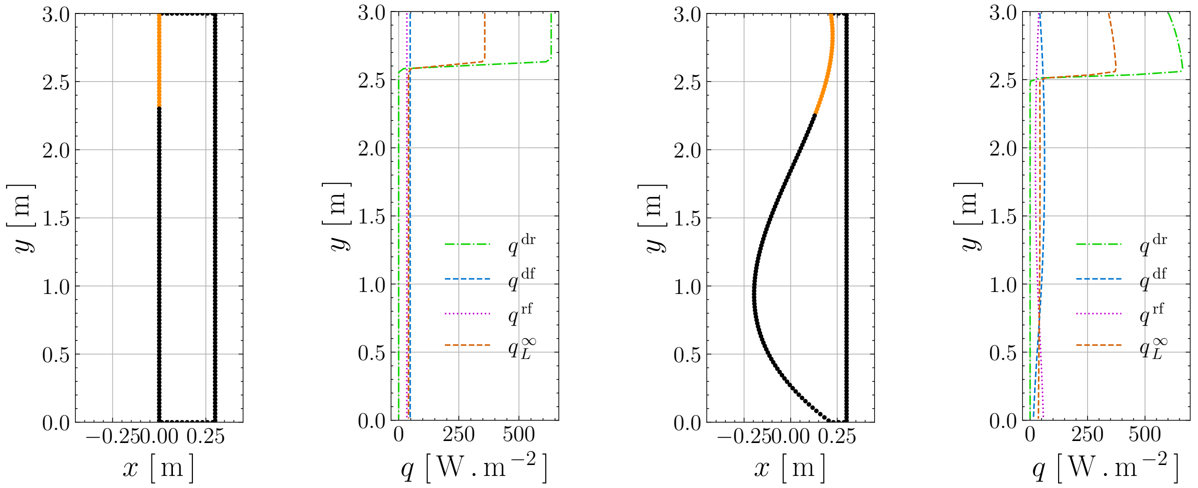

(a) (b) (c) (d)

Figure 11. *Comparison of the reference* (a) *and optimized* (c) *wall shapes with corresponding short wave radiation distributions* (c), (d) *on December 21st at noon for the heat transfer augmentation problem. The orange line* (a,c) *corresponds to the sunlit area.*

Table 4. *Optimized shape parameters according to height and heat conductivity values.*

H [m]	3	3	3	4	5
k [W . m^{-1} . K^{-1}]	0.1	0.5	1	1	1
H/k [W . K^{-1}]	30	6	3	4	5
max $\mathrm{Bi}_L(\boldsymbol{x}^\star)$	351.67	70.33	35.16	49.17	63.85
Bi_R	300	60	30.0	40	50
max $\rho(\boldsymbol{x}^\star)$	1581.73	316.35	158.17	214.37	267.12
p_0°	-1.11	-1.11	-1.11	-0.98	-0.87
p_1°	0.89	0.89	0.89	0.77	0.66

decreased by 12%. Figure 12(c) illustrates that in case of thermal insulation problem optimized shape shows different pattern than in heat transfer augmentation case. The concavity in the middle of the wall creates local shading from the top angle. Thus, it leads to lower short wave radiation influence on the wall.

Another important point regarding the improved wall shapes is that in both cases of heat transfer augmentation and thermal insulation the total area of the wall is the same as in the reference flat case. Thus, from engineering point of view there is no need for additional materials compared to the reference flat wall.

5.4 Results for the whole year

Last, the investigations are performed for the whole domain of zenith angle projection $\theta_z^{'}$ variation in one year (in Nice city) and for different possible values of front building distance/height ratio $\frac{D_x}{D_y}$. Figure 13 illustrates optimized p_0 and p_1 parameters variation for the heat transfer augmentation problems. Similarly, the results for the thermal insulation problems are shown in Figure 14. Note that the parameters estimation was done only inside of the domain where there is a sunlit on the facade and a possibility of significant improvement of the energy efficiency (more that 5 %), as remarked in Section 5.2. As it can be seen from figures there is a lack

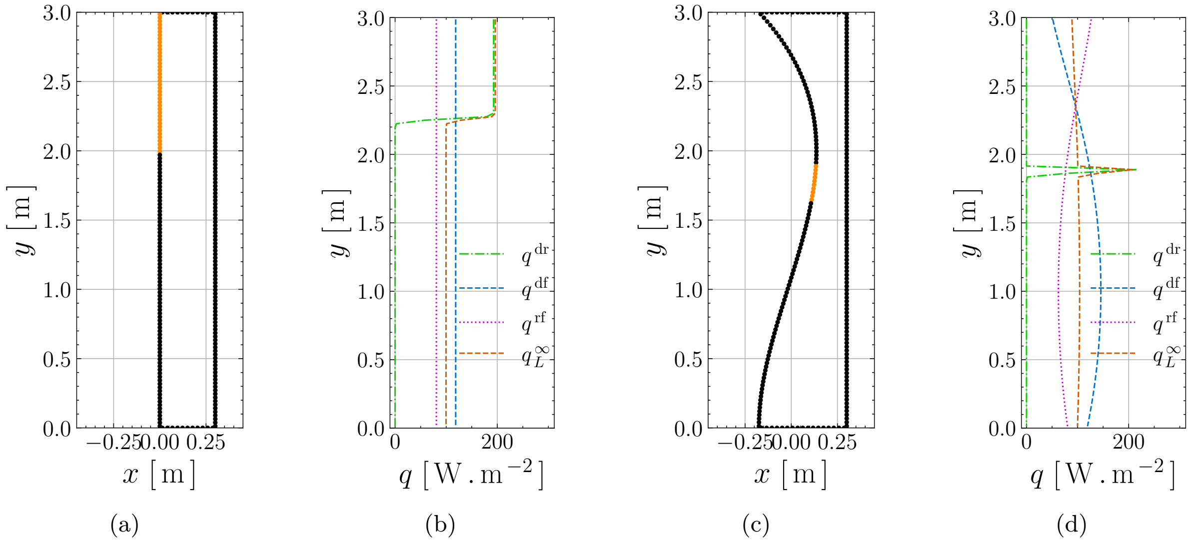

Figure 12. *Comparison of the reference* (a) *and optimized* (c) *wall shapes with corresponding short wave radiation distributions* (b), (d) *on June 21 st at noon for the thermal insulation problems. The orange line* (a,c) *corresponds to the sunlit area.*

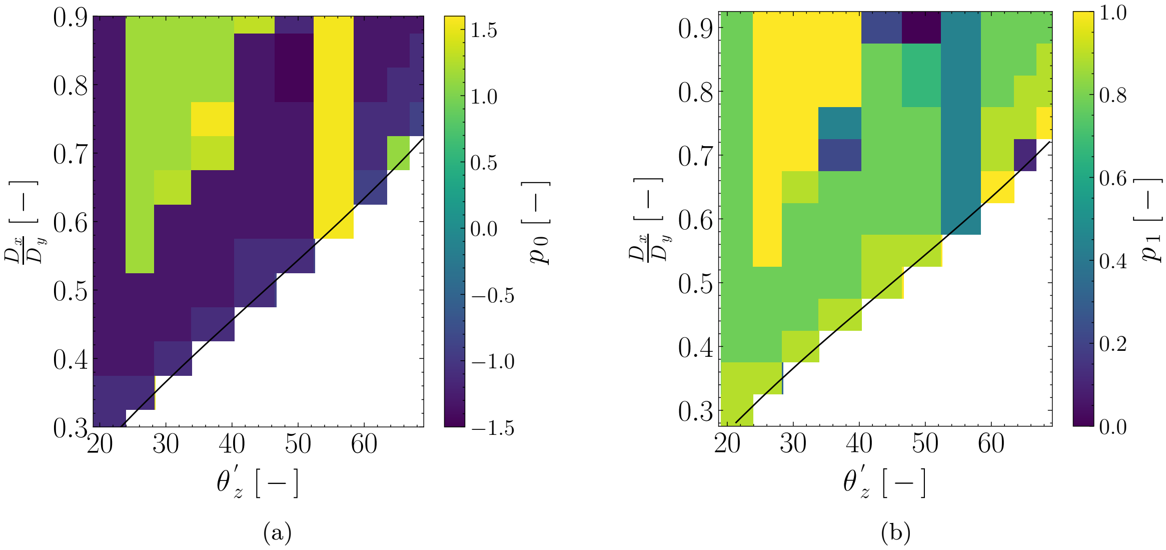

Figure 13. p_0° (a) *and* p_1° (b) *parameters distribution surface for heat transfer augmentation problems.*

of continuity among the optimized parameters, it could be resulted from weak extremum of cost function values. Thus, it will be difficult to deduce parameters pattern on different time periods. As result these diagrams can be used for engineering purposes to construct wall with regard to climate conditions. For instance, engineer interested in decreasing of heat transfer in summer solstice period (June 21 th) with neighbour building's height $D_y = 10.5$ [m] and distance $D_x = 3$ [m]. Therefore, from diagram June 21 th corresponds to $\theta_z' = 18.69^{\circ}$ with a ratio of $D_x / D_y = 0.35$, we obtain $p_0 = -1.15$ and $p_1 = 0$.

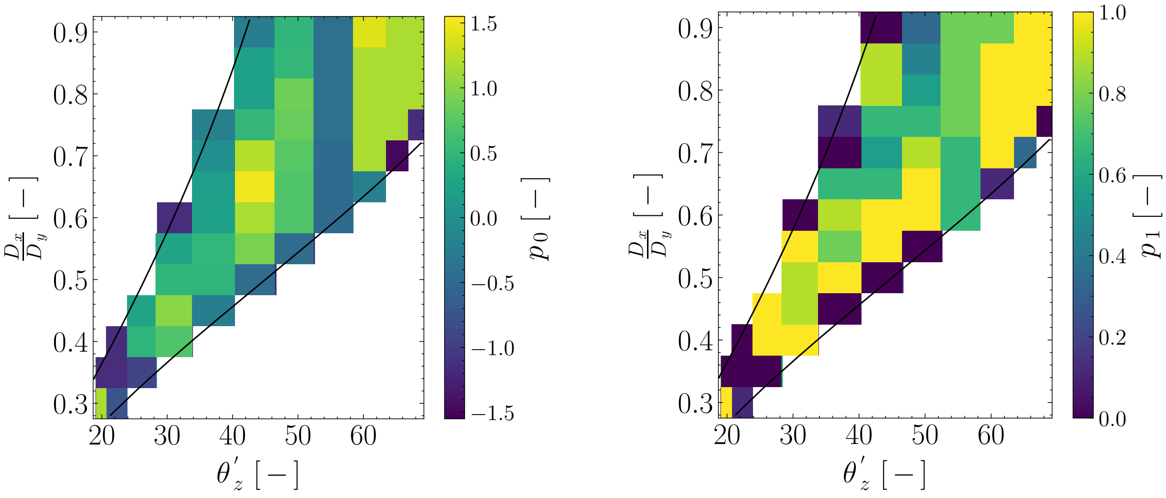

(a) (b)

Figure 14. p_0° (a) *and* p_1° (b) *parameters distribution surface for thermal insulation problems.*

5.5 Further discussion

Since steady-state heat equation is considered at discrete dates throughout the year, it is difficult to choose one shape over another for annual performance. First, lets compare results for December 21st and June 21st at noon in the Table 3. The relative difference ΔJ between optimized and reference cost functions values is chosen as a ratio of benefit. Where ΔJ is defined as:

$$\Delta \mathcal{J} = \left| \frac{\mathcal{J}(\boldsymbol{p}^\circ) - \mathcal{J}(\boldsymbol{p}_{ref})}{\mathcal{J}(\boldsymbol{p}_{ref})} \right| \cdot 100\%.$$

Optimization on December 21st illustrates that benefit $\Delta \mathcal{J} = 732\%$ relative to reference case. Contrary on June 21st ratio of benefit $\Delta \mathcal{J} = 12\%$ from reference case. Results show higher increase of relative benefit on December 21st than on June 21st.

Second, lets see results of ΔJ for whole year. Figure 15 illustrates distribution of ΔJ throughout the year. The average value of ΔJ for the heat transfer augmentation case is equal 49%. Contrary the average value of ΔJ for the thermal insulation is equal 33%. Thus one could assume that it would be favourable to choose optimized shape from heat transfer augmentation case. Since our approach provides an optimized shape for each time instant of the year, one could imagine a mobile facade shape, which adapts each differential area to the changing climate conditions. The mobile facade could smoothly change its shape during the date. For instance Figure 16 illustrates different optimal shapes on December 21st from 9h to 18h and corresponding short wave radiation distribution on Γ_1. If engineer interested in choosing optimal shape for one year, there is a need to consider the transient heat transfer. The transient phenomena are important and authors future research line aims at considering the dynamic phenomena. However, it faces two main issues that are still unsolved.

A first difficulty arises in the definition of the objective (or cost) function. Several indicators have been proposed in the literature as reviewed in [51]. Such proposals are based on temperature difference between inside and outside conditions or on the time integrated heat flux on the inside surface. However, the sense of the thermal flux is completely disregarded but still crucial in transient state. For instance, during a winter day with important incident radiation, an increase of heat transfer is required to provide free heating source to the inside energy balance and occupant thermal comfort. While during the night, the heat transfer through the outside should be minimised. A cost function based on the time integrated heat flux provides an indication of

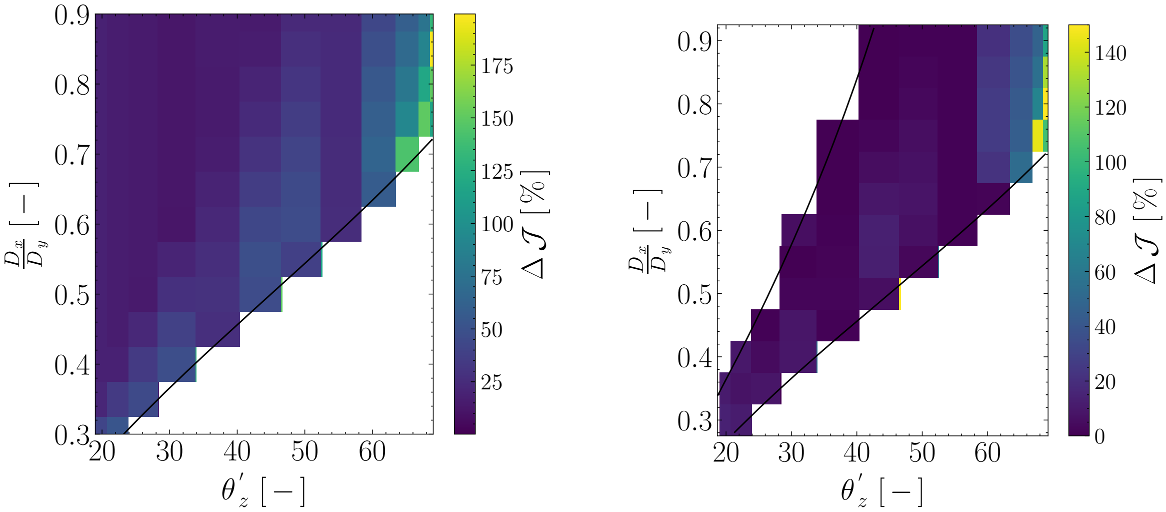

(a) (b)

Figure 15. $\Delta\,\mathcal{J}$ *distribution surface for heat transfer augmentation* (a) *and thermal insulation problems* (b).

the amount of energy leaked through the wall but does not state if this leak is averagely good or bad for the considered period. The phase offset between the outside temperature and the instantaneous heat flux transmitted to the inside zone, is not well integrated in those proposed indicators. In brief, there is no indicator defined for transient and alternative situations of cooling and heating demands. It requires a careful research on this topic before carrying shape optimization in transient state.

Secondly, computational tools combined with building simulation programs have been used in the literature to optimize the energy efficiency of the architectural solutions. However, as noted in Fig.3 of the review from [52], most of the simulations carry parametric designs because computational designs approaches are not adapted to study advanced facade models (through shape and topology optimization of enclosures). Some works have been done considering dynamic enclosures, i.e. with time varying shape [53, 54] or material properties [55]. However, the conclusion of the authors is similar: the actual building simulation tools are limited to design such building envelopes. For instance, in [54], the authors investigate the design of a dynamic external shade based on 2D origami. To carry their investigation, authors cannot model such elements in current building simulations tools so they modify the external schedule solar transmittance on the building enclosure. In [53], a simple steady state heat transfer model. Another review of optimized architectural computational designs is realized in [56]. Most of the methods using optimization focus on non-geometrical parameters such as aggregated thermal parameters of steady state models (as the wall U-value). When dealing with geometric parameters, the size of each layer or the orientation are the design parameters. Out of the 50 references cited in [56], only five carry shape optimization of the whole building enclosure and three for one face of the enclosure (facade or roof). However, in all those approaches, lumped most of them steady state thermal model are considered. Thus, the last drawback is mainly due the modeling of complex transient physical phenomena and its associated computational burden. It requires an efficient numerical strategy to compute fast and accurately the transient two-dimension heat transfer for any shape enclosure.

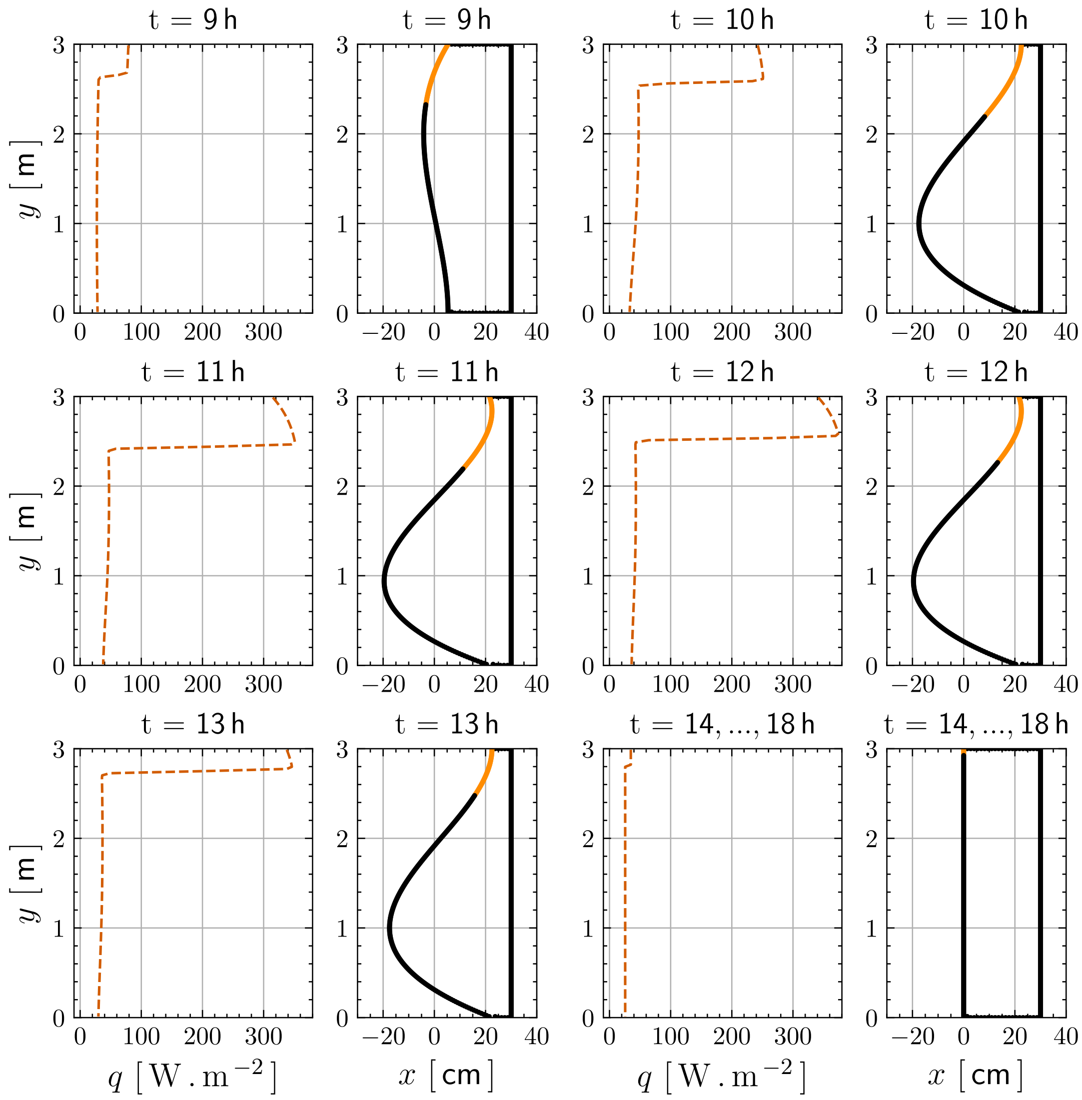

Figure 16. *Illustration of the different shapes on December* 21^{st} *from* 9h *to* 18h.

6 Conclusion

This article investigates wall shape improvement for energy efficiency involving nonuniform incident radiation, which depends on the wall surface shape and orientation. Addition to that the incident short-wave radiation flux is varying according to the height of the facade, due to shadow induce by the urban environment and by the own shape of the wall.

First, the short wave radiation model is defined to predict the magnitude of diffusive, direct and reflective flux according to the height of the facade. Then, the model is verified using a reference solution obtained by pixel counting technique. Calculated results shows a very high consistency with the pixel counting estimations. Second, since the wall shape is in fact a complex geometry domain (not flat), the Boundary Element Method is used for predicting the physical phenomena of steady heat transfer in the two-dimensional wall. Then, the BEM model is verified with analytical solution and compared with the finite difference method. Numerical results highlight that the Boundary Element approach is slightly faster and more accurate than standard finite-difference method, since it only requires discretization of the boundary rather than the entire domain.

Then, a real case study is considered for improvement of the energy efficiency of a building wall. Case study considers a house wall in the south east of France, where the radiation has a high magnitude. Two heat transfer design objectives are defined: *(i)* heat transfer augmentation and *(ii)* thermal insulation. To achieve heat transfer design objectives the wall surface must be sufficiently covered by shadow and sunlit. Thus the domain of improvement values of zenith angle projection and neighbor building distance/height ratio is calculated. Where non shaded area is considered remaining flat wall case scenario. Estimated results meet both goals of heat transfer design objectives without addition of materials. They show that energy efficiency can be improved by 8 times in winter and 12% in summer respectively.

At last, the shape of wall is analysed throughout one year with different height and distance of neighbour buildings. As a result, a diagram of the shape parameters is provided according to day (zenith angle) and position (D_x and D_y) of the neighbour facade. Such tool can be used for engineers to improve the energy efficiency of building facade in the defined area.

Future works should focus on extending the methodology for transient heat and mass transfer taking into account their impact through latent effects. In terms of shape optimization of building enclosures there is a need of investigation of different approaches for wall domain parametrization. Also it will be benefitial to consider numerical modeling in 3D, since it is necessary in many situations because it provides a more accurate representation of real-world phenomena and allows for a more comprehensive analysis compared to 2D modeling. When studying boundary effects, especially in systems with complex boundaries, 3D modeling provides a more accurate representation. For instance, heat transfer in a room with irregularly shaped walls would be better modeled in 3D to capture the effects of all wall surfaces.

7 Acknowledgements

The authors acknowledge the French National Research Agency (ANR) as part of the “JCJC CE-22 AAPG 2023” program (project TOPS) for the financial support.

A Constraints application to the cubic parametrization

Lets consider following third order polynomial:

$$\gamma(\boldsymbol{p}, y) = p_0 y(\frac{y}{H} - p_1)(\frac{y}{H} - 1) + S_{corr}(\boldsymbol{p}),$$

where first term determines the left wall's shape, which is cubic function. A second term is a area corrector S_{corr}, which is added to satisfy the first constraint Eq. 24.

The cubic function has two parameters $\boldsymbol{p} = (p_0, p_1)$, which shapes wall's geometry. It holds zeros at $y = \{0, H\}$. First parameter p_0 describes convexity and concavity of the wall. The function holds third zero proportional to $p_1 \in [0, 1]$.

Area constraint

The first constraint Eq. 24 is satisfied when:

$$\int_{\Gamma_1} p_0 y(\frac{y}{H} - p_1)(\frac{y}{H} - 1)\, d\Gamma + \int_{\Gamma_1} S_{corr}(\boldsymbol{p})\, d\Gamma \geq 0.$$

which means:

$$H\, S_{corr}(\boldsymbol{p}) \geq - \int_{\Gamma_1} p_0 y(\frac{y}{H} - p_1)(\frac{y}{H} - 1)\, d\Gamma.$$

After computation of integrals:

$$S_{corr}(\boldsymbol{p}) \leq \frac{H p_0}{12}(2p_1 - 1).$$

Boundary constraint

The second constraint Eq. 25 is satisfied when:

$$p_0 y(\frac{y}{H} - p_1)(\frac{y}{H} - 1) - \frac{H p_0}{12}(2p_1 - 1) \leq L - \delta,$$

or

$$p_0 \leq \frac{L - \delta}{\left(y(\frac{y}{H} - p_1)(\frac{y}{H} - 1) - \frac{H}{12}(2p_1 - 1)\right)}. \tag{27}$$

Lets denote denominator as:

$$\hat{p}_0(y, p_1) = \left(y(\frac{y}{H} - p_1)(\frac{y}{H} - 1) - \frac{H}{12}(2p_1 - 1)\right).$$

Inequality Eq. 27 needs to be considered for two cases, when $p_0 \geq 0$ and $p_0 \leq 0$.

First case for $p_0 \geq 0$:

For this case Eq. 27 is satisfied when:

$$p_0 \leq \frac{L - \delta}{\min\limits_{y \in [0, H]} \hat{p}_0(y, p_1)}. \tag{28}$$

To find extremum values of the denominator, one needs to consider zeros of its derivative. Thus:

$$\arg \min_{y \in [0, H]} \hat{p}_0(y, p_1) = \hat{y}^+(p_1) = \frac{H}{3}(1 + p_1 - \sqrt{p_1^2 - p_1 + 1}).$$

Eq. 28 can be rewritten as:

$$p_0 \leq \hat{p}_0^+(p_1) \quad \text{where} \quad \hat{p}_0^+(p_1) = \frac{L - \delta}{\hat{p}_0(\hat{y}^+(p_1), p_1)}. \tag{29}$$

Second case for $p_0 \leq 0$:

For this case Eq. 27 is satisfied when:

$$p_0 \leq \frac{L - \delta}{\max\limits_{y \in [0, H]} \hat{p}_0(y, p_1)}. \tag{30}$$

Following same procedure as in the first case to find the extremum values:

$$\arg \max_{y \in [0, H]} \hat{p}_0(y, p_1) = \hat{y}^-(p_1) = \frac{H}{3}(1 + p_1 + \sqrt{p_1^2 - p_1 + 1}).$$

Eq. 30 can be rewritten as:

$$p_0 \geq \hat{p}_0^-(p_1) \qquad \text{where} \qquad \hat{p}_0^-(p_1) = \frac{L - \delta}{\hat{p}_0(\hat{y}^-(p_1), p_1)}. \tag{31}$$

Generalizing the equations 29 and 31:

$$\hat{p}_0^-(p_1) \leq p_0 \leq \hat{p}_0^+(p_1). \tag{32}$$

References

[1] International Energy Agency. Building global energy consumption, 2022. 1

[2] Adriana Ciardiello, Federica Rosso, Jacopo Dell'Olmo, Virgilio Ciancio, Marco Ferrero, and Ferdinando Salata. Multi-objective approach to the optimization of shape and envelope in building energy design. *Applied Energy*, 280:115984, 2020. 1

[3] H.L. Gauch, C.F. Dunant, W. Hawkins, and A. Cabrera Serrenho. What really matters in multi-storey building design? a simultaneous sensitivity study of embodied carbon, construction cost, and operational energy. *Applied Energy*, 333:120585, 2023.

[4] Francisco Toja-Silva, Oscar Lopez-Garcia, Carlos Peralta, Jorge Navarro, and Ignacio Cruz. An empirical–heuristic optimization of the building-roof geometry for urban wind energy exploitation on high-rise buildings. *Applied Energy*, 164:769–794, 2016. 1

[5] Nathan Mendes, Marx Chhay, Julien Berger, and Denys Dutykh. *Numerical methods for diffusion phenomena in building physics: A practical introduction*. 2019. Cited by: 4. 1

[6] Roberto Zanetti Freire, Walter Mazuroski, Marc Olivier Abadie, and Nathan Mendes. Capacitive effect on the heat transfer through building glazing systems. *Applied Energy*, 88(12):4310 – 4319, 2011. Cited by: 40. 2

[7] Julien Berger and Nathan Mendes. An innovative method for the design of high energy performance building envelopes. *Applied Energy*, 190:266 – 277, 2017. 2

[8] Ana Paula de Almeida Rocha, Ricardo C.L.F. Oliveira, and Nathan Mendes. Experimental validation and comparison of direct solar shading calculations within building energy simulation tools: Polygon clipping and pixel counting techniques. *Solar Energy*, 158:462–473, 2017. 2

[9] M. Mirsadeghi, D. Cóstola, B. Blocken, and J.L.M. Hensen. Review of external convective heat transfer coefficient models in building energy simulation programs: Implementation and uncertainty. *Applied Thermal Engineering*, 56(1):134–151, 2013. 2

[10] Nicolas Lauzet, Auline Rodler, Marjorie Musy, Marie-Hélène Azam, Sihem Guernouti, Dasaraden Mauree, and Thibaut Colinart. How building energy models take the local climate into account in an urban context – a review. *Renewable and Sustainable Energy Reviews*, 116:109390, 2019. 2

[11] Mohammad Jafari and Alice Alipour. Methodologies to mitigate wind-induced vibration of tall buildings: A state-of-the-art review. *Journal of Building Engineering*, 33:101582, 2021. 2

[12] Christina Diakaki, Evangelos Grigoroudis, and Dionyssia Kolokotsa. Towards a multi-objective optimization approach for improving energy efficiency in buildings. *Energy and Buildings*, 40(9):1747–1754, 2008. 2

[13] Yunfeng Luo, Wenjiong Chen, Shutian Liu, Quhao Li, and Yaohui Ma. A discrete-continuous parameterization (dcp) for concurrent optimization of structural topologies and continuous material orientations. *Composite Structures*, 236:111900, 03 2020. 2

[14] Yukinori Kametani, Yutaka Fukuda, Takayuki Osawa, and Yosuke Hasegawa. A new framework for design and validation of complex heat transfer surfaces based on adjoint optimization and rapid prototyping technologies. *Journal of Thermal Science and Technology*, 15(2):JTST0016–JTST0016, 2020. 2

[15] Jeong-Tak Jin and Jae-Weon Jeong. Optimization of a free-form building shape to minimize external thermal load using genetic algorithm. *Energy and Buildings*, 85:473–482, 2014. 2

[16] Maryam Asghari Mooneghi and Ramtin Kargarmoakhar. Aerodynamic mitigation and shape optimization of buildings: Review. *Journal of Building Engineering*, 6:225–235, 2016. 2

[17] Shuai Zhang, Dexuan Song, Zhuoyu Yu, Yifan Song, Shubo Du, and Li Yang. Simulation and optimization of insulation wall corner construction for ultra-low energy buildings. *Energies*, 16(3), 2023. 2

[18] Félix Nieto, Miguel Cid Montoya, and Santiago Hernández. Shape optimization of tall buildings cross-section: Balancing profit and aeroelastic performance. *The Structural Design of Tall and Special Buildings*, 31(18):e1982, 2022. 2

[19] Zhaoyong Wang, Chaorong Zheng, Joshua Adriel Mulyanto, and Yue Wu. Aerodynamic shape optimization of a square cylinder with multi-parameter corner recession modifications. *Atmosphere*, 13(11), 2022. 2

[20] José W. Meissner, Marc O. Abadie, Luís M. Moura, Kátia C. Mendonça, and Nathan Mendes. Performance curves of room air conditioners for building energy simulation tools. *Applied Energy*, 129:243 – 252, 2014. 2

[21] Inês Caetano and António Leitão. Architecture meets computation: an overview of the evolution of computational design approaches in architecture. *Architectural Science Review*, 63(2):165–174, 2020. 2

[22] Inês Caetano, Luís Santos, and António Leitão. Computational design in architecture: Defining parametric, generative, and algorithmic design. *Frontiers of Architectural Research*, 9(2):287–300, 2020. 2

[23] Longwei Zhang, Chao Wang, Yu Chen, and Lingling Zhang. Multi-objective optimization method for the shape of large-space buildings dominated by solar energy gain in the early design stage. *Frontiers in Energy Research*, 9, 2021. 2

[24] Maryam Talaei, Mohammadjavad Mahdavinejad, Rahman Azari, Alejandro Prieto, and Hamed Sangin. Multi-objective optimization of building-integrated microalgae photobioreactors for energy and daylighting performance. *Journal of Building Engineering*, 42:102832, 2021.

[25] Jérôme Henri Kämpf, Marylène Montavon, Josep Bunyesc, Raffaele Bolliger, and Darren Robinson. Optimisation of buildings' solar irradiation availability. *Solar Energy*, 84(4):596–603, 2010. International Conference CISBAT 2007.

[26] Reza Fallahtafti and Mohammadjavad Mahdavinejad. Optimisation of building shape and orientation for better energy efficient architecture. *International Journal of Energy Sector Management*, 9:593–618, 11 2015. 2

[27] Abdollah Baghaei Daemei and Seyed Eghbali. Study on aerodynamic shape optimization of tall buildings using architectural modifications in order to reduce wake region. *Wind and Structures An International Journal*, 29:139–147, 08 2019. 2

[28] Jeong-Tak Jin and Jae-Weon Jeong. Thermal characteristic prediction models for a free-form building in various climate zones. *Energy*, 50:468–476, 2013. 3

[29] Magdi Rashad, Alina Żabnieńska Góra, Les Norman, and Hussam Jouhara. Analysis of energy demand in a residential building using trnsys. *Energy*, 254:124357, 2022. 3

[30] Mayssa Dabaghi Aram Yeretzian, Hmayag Partamian and Rabih Jabr. Integrating building shape optimization into the architectural design process. *Architectural Science Review*, 63(1):63–73, 2020. 3

[31] Longwei Zhang, Lingling Zhang, and Yuetao Wang. Shape optimization of free-form buildings based on solar radiation gain and space efficiency using a multi-objective genetic algorithm in the severe cold zones of china. *Solar Energy*, 132:38–50, 2016.

[32] Rabee M. Reffat and Radwa Ezzat. Impacts of design configurations and movements of pv attached to building facades on increasing generated renewable energy. *Solar Energy*, 252:50–71, 2023. 3

[33] Modeste Kameni Nematchoua, Jean Christophe Vanona Noelson, Ismaïl Saadi, Herves Kenfack, Aro-Zo F.R. Andrianaharinjaka, Dominique Foumouo Ngoumdoum, Jao Barahimo Sela, and Sigrid Reiter. Application of phase change materials, thermal insulation, and external shading for thermal comfort improvement and cooling energy demand reduction in an office building under different coastal tropical climates. *Solar Energy*, 207:458–470, 2020. 3

[34] Rustu Eke and Cihan Demircan. Shading effect on the energy rating of two identical pv systems on a building façade. *Solar Energy*, 122:48–57, 2015. 3

[35] Jaewon Kim, Hyomun Lee, Mungyu Choi, Dongsu Kim, and Jongho Yoon. Power performance assessment of pv blinds system considering self-shading effects. *Solar Energy*, 262:111834, 2023. 3

[36] Wenxian Lin, Jidong Yi, A.L. Graham, Tao Liu, Chaofeng Xia, M.S. Ingber, J.W. Leggoe, and J.R. Abbott. Boundary-element method simulation of the impact of bounding walls on the dynamics of a particle group freely moving in a wide-gap couette flow. *Applied Energy*, 83(7):669–680, 2006. 3

[37] Louis S.H. Lee and C.Y. Jim. Energy benefits of green-wall shading based on novel-accurate apportionment of short-wave radiation components. *Applied Energy*, 238:1506–1518, 2019. 4

[38] W. H. McAdams. *Heat Transmission.* 1985. 4

[39] Efim G. Evseev and Avraham I. Kudish. The assessment of different models to predict the global solar radiation on a surface tilted to the south. *Solar Energy*, 83(3):377–388, 2009. 5

[40] Soteris Kalogirou. *Solar Energy Engineering: Processes and Systems: Second Edition.* 01 2009. 5

[41] Benjamin Y.H. Liu and Richard C. Jordan. The interrelationship and characteristic distribution of direct, diffuse and total solar radiation. *Solar Energy*, 4(3):1–19, 1960. 6, 7

[42] Seyyed Mohsen Mortazavinejad and Milad Mozafarifard. Numerical investigation of two-dimensional heat transfer of an absorbing plate of a flat-plate solar collector using dual-reciprocity method based on boundary element. *Solar Energy*, 191:332–340, 2019. 9

[43] L. Marin. Numerical boundary identification for helmholtz-type equations. *Computational Mechanics*, 39:25–40, 12 2006. 9

[44] M. H. Aliabadi L. C. Wrobel. *The Boundary Element Method, Volume 1: Applications in Thermo-Fluids and Acoustics.* Wiley–Blackwell, 2002. 10

[45] Zongyi Xing, Zhenyu Zhang, Jian Guo, Yong Qin, and Limin Jia. Rail train operation energy-saving optimization based on improved brute-force search. *Applied Energy*, 330:120345, 2023. 12

[46] Nathaniel Jones, Donald Greenberg, and Kevin Pratt. Fast computer graphics techniques for calculating direct solar radiation on complex building surfaces. *Journal of Building Performance Simulation*, 5:300–312, 09 2012. 12

[47] Ana Paula de Almeida Rocha, Gilberto Reynoso-Meza, Ricardo C.L.F. Oliveira, and Nathan Mendes. A pixel counting based method for designing shading devices in buildings considering energy efficiency, daylight use and fading protection. *Applied Energy*, 262, 2020. 12

[48] Ana Paula de Almeida Rocha, Auline Rodler, Ricardo C.L.F. Oliveira, Joseph Virgone, and Nathan Mendes. A pixel counting technique for sun patch assessment within building enclosures. *Solar Energy*, 184:173 – 186, 2019. 12

[49] Payam Shafigh, Iman Asadi, Amir Akhiani, Norhayati Mahyuddin, and Mohammad Hashemi. Thermal properties of cement mortar with different mix proportions. *Materiales de Construcción*, 70, 07 2020. 16

[50] Meteonorm Software. Global climate database, 2020. 18

[51] G. Barrios, G. Huelsz, J. Rojas, J. M. Ochoa, and I. Marincic. Envelope wall/roof thermal performance parameters for non air-conditioned buildings. *Energy and Buildings*, 50:120–127, 2012. 21

[52] I. Caetano, L. Santos, and A. Leitão. Computational design in architecture: Defining parametric, generative, and algorithmic design. *Frontiers of Architectural Research*, 9(2):287–300, 2020. 22

[53] J. Grinham, S. Craig, D.E. Ingber, and M. Bechthold. Origami microfluidics for radiant cooling with small temperature differences in buildings. *Applied Energy*, 277:115610, 2020. 22

[54] H. Kim and M.J. Clayton. Parametric behavior maps: A method for evaluating the energy performance of climate-adaptive building envelopes. *Energy and Buildings*, 219:110020, 2020. 22

[55] S. Craig and J. Grinham. Breathing walls: The design of porous materials for heat exchange and decentralized ventilation. *Energy and Buildings*, 149:246–259, 2017. 22

[56] B. Ekici, C. Cubukcuoglu, M. Turrin, and I.S. Sariyildiz. Performative computational architecture using swarm and evolutionary optimisation: A review. *Building and Environment*, 147:356–371, 2019. 22